Reactive transport modeling of leaking CO_2-saturated brine along a fractured pathway

Nawaz Ahmad[a,b,*], Anders Wörman[a], Andrea Bottacin-Busolin[c], and Xavier Sanchez-Vila[d]

[a] Department of Civil and Architectural Engineering, KTH Royal Institute of Technology, Brinellvägen 23, 10044, Stockholm, Sweden

[b] Policy Wing, Ministry of Petroleum and Natural Resources, Islamabad, Pakistan

[c] School of Mechanical, Aerospace and Civil Engineering, University of Manchester, United Kingdom

[d] Hydrogeology Group, Department of Geotechnical Engineering and Geosciences, Universitat Politècnica de Catalunya, UPC-BarcelonaTech, 08034 Barcelona, Spain

*Corresponding author: Nawaz Ahmad, Department of Civil and Architectural Engineering, KTH Royal Institute of Technology, Brinellvägen 23, 10044, Stockholm, Sweden.

Email: nawaza@kth.se

Tel: +46 8 7909261

ABSTRACT

One concern regarding the underground storage of carbon dioxide (CO_2) is its potential leakage from reservoirs. Over short period of time, the leakage risk is related mainly to CO_2 as a separate supercritical fluid phase. However, over longer periods upon complete dissolution of injected CO_2 in the fluid, the leakage risk is associated with dissolved phase CO_2. Over the geological time scales, large-scale groundwater motion may cause displacement of brine containing dissolved CO_2 along the conducting pathways. In this paper, we present a comprehensive modeling framework that describes the reactive transport of CO_2-saturated brine along a fracture in the clay caprock based on the future, hypothetical leakage of the dissolved phase CO_2. This study shows that the transport of leaked dissolved CO_2 is significantly retarded by a combination of various physical and geochemical processes, such as mass exchange between conducting fracture and the neighboring rock matrix through molecular diffusion, sorption and calcite dissolution in the rock matrix. Mass stored in aqueous and adsorbed states in the rock matrix caused retention of dissolved CO_2 along the leakage pathway. Calcite dissolution reaction in the rock matrix resulted in consumption of leaking dissolved CO_2 and reduced its mass along the leakage pathway. Consumption and retention of dissolved CO_2 along the leakage pathway have important implications for analyzing the potential reduction of CO_2 fluxes from storage reservoirs over large periods and long travel pathways.

Keywords: CO_2-saturated brine leakage, Reactive transport, Fracture, Matrix diffusion, Sorption, Calcite kinetic reaction

Contents

1. Introduction

The CO_2 geological sequestration has been proposed for mitigating the imbalance of gas emissions (Holloway, 1997, 2005; IPCC, 2002; Middleton et al., 2012). CO_2 is injected in deep subsurface geological reservoirs in a dense supercritical state (IPCC, 2005). Due to its lower density compared to the resident brine, the injected CO_2 tends to accumulate towards the top of the reservoir (Arts et al., 2005; Audigane et al., 2005; Pruess, 2006(a); Orr, 2009). Over short periods (up to 100 years), CO_2 is stored as a separate fluid phase (CO_{2g}) in the reservoir (physical trapping) (Audigane et al., 2005). However, CO_{2g} dissolves in the formation brine at the brine-CO_{2g} interface (solubility and ionic trapping) (Orr, 2009; IPCC, 2005). The resulting CO_2–saturated brine becomes slightly denser with respect to its original value, which causes gravity-driven downward flow, produces fingering, enhances fluids mixing, and increases CO_{2g} dissolution (Audigane et al., 2007). It might take almost 10,000 years for complete dissolution of injected CO_{2g} into the formation fluid (Audigane et al., 2005, 2007). Dissolution of CO_{2g} in the formation fluid lowers the pH of the resulting brine, driving heterogeneous geochemical reactions that result in fixation of CO_2 through precipitation of carbonate minerals (Audigane et al., 2005; Gunter et al., 1993). This process, termed mineral trapping, dominates over thousands to millions of years (Gunter et al., 1993; IPCC, 2005).

One concern related to the underground storage of CO_{2g} is its potential to leak from the storage reservoir (Haugan & Joos, 2004; Pruess, 2005; Stone et al., 2009). As long as injected CO_{2g} stays as a separate fluid phase in the reservoir (tens of years), higher leakage risk exists due to its lower density as compared to the resident fluid (Pruess, 2006a, 2006b). At large times, upon complete dissolution of CO_{2g} in the formation fluid, leakage risk is associated to the presence of CO_2 in dissolved phase (Bachu et al., 1994). Audigane et al., 2007 found that all the injected CO_{2g} was completely dissolved in the formation fluid after 10,000

116 years whereas only 5% was consumed through mineral reactions. Thus, after thousands
117 of years, only CO_2-saturated brine in the reservoir is expected, and the risk for
118 leakages of CO_2 is associated only with its dissolved phase (CO_{2aq}).
119 Large-scale groundwater motion may cause bulk displacement of brine out of the
120 reservoir with associated CO_{2aq} leakage risk (Bachu et al., 1994; IPCC, 2005; Gaus,
121 2010). In the sedimentary basins, groundwater flow velocities can be expected on the order of
122 millimeters to centimeters per year (Bachu et al., 1994). Thus due to low groundwater
123 velocities the leakage risk of CO_{2aq} is substantially lower than that of CO_{2g}. Transport of
124 CO_{2aq} may take place by advection, dispersion and diffusion processes (Bachu et al., 1994).
125 Although fractures act as the principal conductors for flow, the neighboring rock matrix also
126 plays a significant role in the solute transport processes (Grisak & Pickens, 1980). The
127 reactive species that diffuse from the fractures into the matrix may undergo sorption on the
128 surface of the solid and may react with the minerals in the rock matrix, which would
129 significantly inhibit the transport of reactive or non-reactive species in fractured rocks (Bodin
130 et al., 2003; Cvetkovic et al., 1999; Neretnieks, 1980; Xu et al., 2001). Thus, the interplay
131 between the conducting fracture and the matrix through diffusion is important for
132 understanding the transport of leaking CO_2-saturated brine.
133 Particularly, along the transport pathway, CO_{2aq} may undergo physical and geochemical
134 interactions with the existing rock formation minerals. These CO_2-rock interactions can
135 enhance transport by increasing hydraulic conductivity, linked to the porosity increases
136 caused by mineral dissolution, or decrease transport by decreasing the permeability due to
137 mineral precipitation. For example, a carbonate mineral filling the fracture could dissolve and
138 widen the existing flow path (Gaus, 2010). Calcite dissolution and precipitation along the
139 leakage pathway may result in a net conversion and uptake of CO_{2aq}. Kaufmann &
140 Dreybrodt, 2007 have reported the conversion of CO_{2aq} due to calcite dissolution in a ternary

141 $CaCO_3$-H_2O-CO_2 system. This indicates the relevance of studying the physical and
142 geochemical interactions of leaking CO_2-saturated brine in rock formations along the flow
143 pathway.
144 To date, no studies have been published in which retention and consumption of CO_{2aq} is
145 analyzed based on a physico-geochemical formulation of coupling transport in fractures,
146 molecular diffusion in the porous rock matrix (matrix diffusion) and reactions on available
147 rock surfaces in the matrix. So far, only few experimental and relatively simple numerical
148 modeling studies have been published related to the leakage of dissolved CO_2 (Gaus, 2010).
149 Gherardi et al., 2007 performed numerical simulations of the geochemical interactions of
150 caprock with leakage of the CO_2 gas phase and the associated brine simultaneously. These
151 authors found that calcite dissolution or precipitation was the most significant process that
152 controlled the chemical evolution of the caprock and responsible for changes in the porosity
153 near the reservoir-caprock interface. Ellis et al., 2011 conducted a seven-day experiment to
154 investigate the evolution of a fractured carbonate caprock due to geochemical interactions
155 with leaking CO_2-acidified brine. Andreani et al., 2008 reported experimental studies
156 regarding the fracture evolution due to cyclic flows of CO_2 dissolved in brine and the free-
157 phase CO_2. These authors reported an increase in porosity of 50% near the fracture, mainly
158 due to calcite dissolution. Nogues et al., 2013 analyzed the evolution of medium porosity and
159 pore-scale permeability caused by inflowing CO_2-saturated water. These authors concluded
160 that the geochemical modeling could be simplified by not including the reactions of minerals
161 kaolinite, anorthite, and albite whenever carbonate minerals are abundant. Peters et al., 2014
162 reported that a complex set of factors and processes are involved in permeability variations
163 resulting from dissolution of calcite in the caprock flow pathways caused by acidified brine
164 containing CO_{2aq}. These authors recommend including the complex geochemical interactions

of CO_2-saturated brine with calcite into reactive transport models to properly predict the flow paths' permeability evolution.

The aim of the present study is to provide a quantitative understanding of the transport of CO_2-saturated brine along fractured pathways, leaking from deep storage reservoir caused by large-scale groundwater flow over geological time scales. This study analyzes the retention and consumption of CO_{2aq} due to various physical and geochemical processes in the rock matrix adjacent to the main flow conducting pathway. In this study we present a comprehensive reactive transport model capable of analyzing the evolution of porosity along the leakage pathway due to dissolution and precipitation of calcite over the period of time. The novel approach adopted here explicitly couples the relatively fast transport of CO_{2aq} in the fracture with slow transport in the neighboring rock matrix through molecular diffusion, while accounting for various physical and geochemical processes, such as sorption, various aqueous phase equilibria, and calcite mineral kinetic reactions in the rock matrix.

The full system of equations describing the reactive transport in terms of the chemical components is presented here in a comprehensive form that can be efficiently solved using numerical methods. The model framework is applied to a scenario that is believed to represent the leakage of CO_{2aq} in a brine solution that is slowly flowing through a fracture in a clayey caprock caused by regional-scale groundwater motion. Various transport scenarios are performed over a period of 500 years to evaluate the significance of various physical and geochemical processes on the mobility and consumption of CO_{2aq} in geochemical reactions along the leakage pathway. Sensitivity analysis is then performed to analyze the effects of various parameters (i.e. advective velocity in the fracture, sorption partition coefficient, pressure and temperature conditions, and diffusion coefficient) on the retention and consumption of CO_{2aq} along the leakage pathway. Comparative analysis between various reactive transport scenarios is presented in terms of variations in medium porosity, retention

of CO_{2aq} caused by mass stored in aqueous and adsorbed states, mass uptake of CO_{2aq} in geochemical reactions, and transport retardation along the leakage pathway.

2. Mathematical and numerical model

2.1. Numerical solution technique

The batch and the reactive transport modeling are performed in COMSOL Multiphysics that is based on the finite element method. Fast aqueous phase reactions are modeled as equilibrium reactions governed by the law of mass action. In contrast, the kinetics of calcite mineral are considered slow and modeled as kinetically controlled. Aqueous phase reactions are considered in both the fracture and the surrounding rock matrix whereas mineral kinetic reactions are considered only in the rock matrix. In this study the concentration of chloride (Cl^-) is taken equal to a constant value of 0.5 mol/(kg water) by considering it as a conservative solute that does not participate in any of the geochemical reactions.

In this study the transport problem and the geochemistry are solved in a partially coupled mode. Transport of aqueous species in the conducting fracture is modeled through the advection-dispersion-reaction transport equation, whereas diffusion and reaction are considered as the transport processes in the rock matrix. While considering a constant velocity in the fracture, the transport processes in the fracture are modeled independently of variations in porosity and permeability taking place in the rock matrix. Aqueous phase equilibrium reactions are considered in conducting fracture and neighbouring rock matrix, however calcite dissolution and precipitation is only considered in the rock matrix. This simplification seems reasonable for a constant fluid velocity taken in the fracture. Diffusion in the rock matrix is characterized by an effective diffusivity, being a function of porosity of the rock matrix, and thus varying in time

and space caused by geochemical reactions. Further the mineral kinetic reactions in the rock matrix are modeled as a function of medium porosity and mineral reactive surface area that also vary in time and space. Spatial and temporal variations in minerals' reactive surface area, medium porosity and permeability in the rock matrix are updated based on the minerals dissolution/precipitation.

The mass conservation of aqueous species is formulated in terms of chemical component species (u) that are linear combination of aqueous species (c) (Yeh & Tripathi, 1991; Steefel & Lasaga, 1994). The methodology is presented by Saaltink et al., 1998 (Appendix A). The consumption or production of chemical components in the transport equation appears through the reaction term that represents the combined effect of aqueous phase equilibrium and mineral kinetic reactions. In this study, the equilibrium state obtained from the numerical solution of the background batch geochemical modeling is used as initial conditions in the subsequent transport modeling. This way, the solution of transport system requires only specifying the boundary conditions in terms of chemical components.

Time-marching is performed by using an implicit nonlinear solver based on the backward differentiation formula (BDF) with the Jacobian matrix updated at each iteration. The variables are solved using a segregated solver technique that splits the solution process into sub-steps, each one having individual numerical settings. In the segregated technique the iteration process is continued until convergence. All the solution sub-steps used the damped version of Newton's method with all damping factors set equal to unity. The transport equation and the system of algebraic equations required for speciation are solved together in segregated step-1. The ordinary

239 differential equation (ODE) required for mass conservation of kinetically controlled
240 minerals is solved in segregated step-2.

241 *2.2. Geochemical system for brine-rock interactions*

242 The set of geochemical reactions that describe the brine-rock chemical interactions is
243 presented in Table 1. Five of the reactions ((R0) through (R4)) represent aqueous phase
244 equilibrium reactions whereas the last reaction (R5) represents the kinetic reaction of
245 mineral calcite. The reaction (R0) that represents the equilibrium between CO_{2g} and
246 CO_{2aq} is only considered in the batch geochemical modeling. This reaction is excluded
247 in the subsequent reactive transport modeling due to the fact that CO_{2g} is not modeled.
248 In this study, the solubility model of Duan & Sun, 2003 (modified by Duan et al., 2006) is
249 used to model the dissolution of injected CO_{2g} in the saline water (0.5 M NaCl). This
250 solubility model is valid for a wide range of temperatures, pressures and ionic
251 strengths, that also takes into account the effects of dissolved species Na^+, Cl^-, K^+,
252 Ca^{2+}, Mg^{2+}, and SO_4^{2-}. The equilibrium constants for the reactions ((R1) through (R5))
253 are calculated as a function of temperature and are based on the default thermodynamic
254 database of "The Geochemist's Workbench (GWB)".

255

256 **Table 1.** Chemical reactions considered for $CaCO_3$-H_2O-CO_2 system.

No.	Reactions and equilibrium reaction constants
(R0)[1]	$CO_{2g} \leftrightarrow CO_{2aq}$
(R1)[2]	$H_2O + CO_{2aq} \leftrightarrow H^+ + HCO_3^-$
(R2)[2]	$H_2O \leftrightarrow H^+ + OH^-$
(R3)[2]	$HCO_3^- \leftrightarrow H^+ + CO_3^{2-}$
(R4)[2]	$Na^+ + HCO_3^- \leftrightarrow NaHCO_{3aq}$
(R5)[2]	$CaCO_3 + H^+ \leftrightarrow Ca^{2+} + HCO_3^-$

257 1. Equilibrium reaction constant is based on Duan & Sun, 2003 as modified by Duan et al.,
258 2006; 2. Equilibrium reaction constants are taken from The Geochemist's Workbench (GWB)
259 (default thermodynamic data for the GWB).

2.3. Batch geochemical modeling (BGM)

2.3.1. Background BGM

Before performing the reactive transport modeling the equilibrated geochemical conditions in the transport domain are obtained from the background BGM. Background BGM is also performed for the reservoir to know the geochemical conditions under natural conditions prior to dissolution modeling of injected CO_{2g}. The background BGM is performed for water-rock interactions at a temperature of 45°C and a CO_2 partial pressure (P_{CO_2}) of 0.01 bar until equilibrium with respect to mineral calcite is reached. During subsequent reactive transport modeling, the equilibrated water chemistry obtained from the background BGM in the transport domain ensures that the reactivity can be attributed solely to the concentrations of the dissolved species in the CO_2-saturated brine leaking from the deep storage reservoir.

2.3.2. CO_{2g} dissolution reaction modeling in the reservoir

The water chemistry resulting from the background BGM is used as an initial condition for CO_{2g} dissolution reaction modeling. The CO_{2g} dissolution reaction modeling is performed at a temperature of 45°C and at a pressure of 105 bar (Gherardi et al., 2007). These values are representative of the conditions expected at top boundary of the reservoir at a depth of 1040 m below the land surface for assumed pressure and temperature gradient of 0.1 bar/m and 0.03 °C/m below the land surface (Pruess, 2008). In CO_{2g} dissolution reaction modeling, partial pressure of CO_{2g} is increased to 105 bar from its background pressure of 0.01 bar. The resulting water chemistry from the CO_{2g} dissolution reaction modeling is used as a boundary condition for the subsequent reactive transport modeling.

2.4. Reactive transport

2.4.1. Conceptual transport model

The conceptual transport model presented in Figure 1 shows the CO_2 storage reservoir (bottom) and the clayey caprock (top). Only the fracture-matrix system in the clayey caprock

overlying the deep geological reservoir is included in the transport simulations. Assuming no material fill-ins, porosity of the conducting fracture is taken as unity. In the coupled fracture-matrix system, W_f is the half-fracture spacing, W_m is the matrix width and L is the length of the fracture and the matrix. Symmetry is assumed at the left boundary (center of the fracture) and right boundary of the rock matrix. The sizes of the modeled transport domain are arbitrarily taken as L= 20 m, W_f= 1 mm, and W_m= 10 m. For the base-case transport scenarios, a constant fluid vertical velocity of 3.171×10^{-7} m/s (10 m/year) is used in the fracture, whereas velocity is assumed to be zero in the rock matrix. This velocity magnitude in the fracture is considered representative of Darcy's velocities on the order of 1 to 10 cm/year for large-scale groundwater motion in bedrock continuum formed by the deep sedimentary basins reported by Bachu et al., 1994. The considered length (20 m) of the transport pathway is believed to be relevant for the considered flow velocity in the fracture and for a simulation time of 500 years. The initial porosity of the rock matrix (clayey caprock) of 12% is selected from the mineralogical composition reported in Table 2.

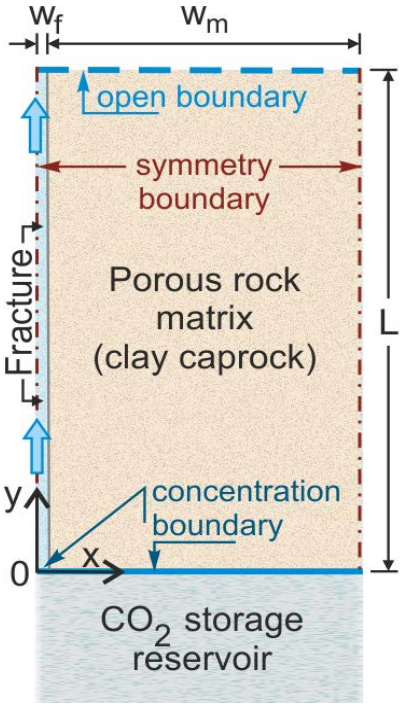

Figure 1. Schematic of the transport domain (clayey caprock containing a vertical fracture) lying above the CO_2 geological storage reservoir.

Table 2. Clay caprock mineralogical composition (Gherardi et al., 2007).

Minerals	Volume fraction in solid rock	Volume fraction in porous rock (12% porosity)
Calcite	0.29	0.255
Dolomite	0.04	0.035
Quartz	0.20	0.176
Illite	0.02	0.018
K-feldspar	0	0
Chlorite	0.06	0.053
Albite	0	0
Kaolinite	0.05	0.044
Na-smectite	0.15	0.132
Muscovite	0.19	0.1672

2.4.2. Reactive transport system for mobile species

Reactive flow and transport modeling is performed for a single-phase CO_2-saturated brine that also contains other species. The solute transport in the fracture-matrix system can be conceptualized as a dual-domain system, where the transport along the fracture is driven by advection, dispersion and diffusion whereas, in the matrix, transport only occurs by diffusion (Steefel & Lichtner, 1998a, 1998b; Novak, 1993, 1996). The following reactive transport equation, for multiple dissolved species (mobile ones) in a single aqueous phase and time dependent porosity, is used (COMSOL):

$$\mathbf{R_f}\theta\frac{\partial \mathbf{c}}{\partial t} + \left(1 - \mathbf{K_d}\rho_p\right)\mathbf{c}\frac{\partial \theta}{\partial t} - \nabla\cdot[(\mathbf{D_D} + \mathbf{D_e})\nabla\mathbf{c}] + \nabla\cdot(\mathbf{vc}) = \theta\mathbf{r_{kin}} \quad (1)$$

In the above equation $\nabla = (\partial/\partial x, \partial/\partial y)$ is Nabla operator; $\theta(x,y,t)$ is the porosity (updated in space and time) of the rock matrix; $\mathbf{c}(x,y,t)$ is a vector of the concentration [mol/(kg water)] of all aqueous species; $\rho_p(x,y,t)$ is the particle density [kg/m^3] of the rock formation; $\mathbf{D_D}$ is the dispersion tensor [m^2/s]; $\mathbf{D_e} = \theta\mathbf{D_b}$ is the effective diffusion (diagonal) tensor [m^2/s] defined as a function of medium porosity with $\mathbf{D_b}$ is a tensor of diffusion coefficients of the involved species; $\mathbf{v}(x,y,t)$ is the Darcy's velocity vector [m/s] (pore velocity times porosity); $\mathbf{r_{kin}}(x,y,t)$ is the sink/source [mol/(s kg water)] term in vector form

that represents consumption/production of species due to all of the geochemical reactions (aqueous phase equilibrium as well as calcite kinetics) and $\mathbf{R_f}$(x,y,t) is a diagonal matrix of retardation factors due to sorption of mobile species on the surface of immobile mineral phases.

The order of this reactive transport system can be reduced by expressing the species concentration vector (**c**) in term of chemical components concentration vector (**u**). The procedure for expressing the species concentration in terms of the chemical components for reducing the order of the reactive transport system is presented in Appendix A. Following this procedure, we present the reactive transport equation (1) in terms of the chemical components concentration (**u**) as follows:

$$\mathbf{R_f}\theta\frac{\partial \mathbf{u}}{\partial t} + \left(1 - \mathbf{K_d}\rho_p\right)\mathbf{u}\frac{\partial \theta}{\partial t} - \nabla\cdot[(\mathbf{D_D} + \mathbf{D_e})\nabla\mathbf{u}] + \nabla\cdot(\mathbf{vu}) = \theta\mathbf{r_{kin}} \quad (2)$$

where the retardation factor due to sorption of mobile species on the surface of immobile rock matrix is defined by the following relation (COMSOL):

$$\mathbf{R_f} = 1 + \frac{\rho_{bulk}}{\theta}\mathbf{K_d} \quad (3)$$

In equation (3), $\rho_{bulk} = (1-\theta)\rho_p$ is the bulk density [kg/(m^3 bulk volume)] of the porous rock matrix defined as a function of porosity of the medium and $\mathbf{K_d}$(x,y,t) represents a diagonal matrix whose diagonal elements are the sorption partition coefficients [m^3/kg] of the involved component species. Using the component form, the reactive transport system defined by equations (2) and (3) now involves only four components rather than the eight species involved in the original system (Appendix A). Therefore vector **u** in equation (2) has 4 components whereas $\mathbf{R_f}$ and $\mathbf{K_d}$ are 4×4 matrices. The transport equation (2) is a nonlinear partial differential equation in which all the variables (θ, θ_p, θ_{bulk}, $\mathbf{D_e}$, the matrices $\mathbf{K_d}$ and $\mathbf{R_f}$ as well as the vector $\mathbf{r_{kin}}$) are nonlinear function of the local concentration of component species (**u**) and are thus updated in time and

space. The reaction term ($\mathbf{r_{kin}}$) represents the consumption or production of component species due to the combined effects of all geochemical reactions.

2.4.3. Mass conservation of mineral phases (immobile species)

The mass conservation of minerals (considered as immobile) undergoing kinetic reactions is modeled using the following ODE:

$$\frac{\partial \mathbf{c_{m,bulk}}}{\partial t} = -\theta \rho_b \mathbf{r_m} \qquad (4)$$

where $\mathbf{c_{m,bulk}}$(x,y,t) is a vector of mass of all kinetically controlled minerals expressed as mol/(m^3 bulk volume) which is calcite alone in this study; $\rho_b$is the fluid density taken equal to 1000 kg/m^3; $\mathbf{r_m}$ (x,y,t) is a vector representing the consumption or production [mol/(s kg water)] of the mineral phases due to their kinetically controlled reaction (equation 5). The initial values of mineral mass ($c_{m,bulk}$) are calculated from their initial volume fractions in the porous rock matrix.

2.4.4. Minerals kinetic reaction (dissolution/precipitation)

Slow mineral reactions are characterized by the kinetic reaction rate (r_m), which is defined as the rate of conversion of the reactants into products per unit time and kg of water. The kinetically controlled reaction of minerals is defined as a function of mineral reaction rate constant, the concentration of aqueous species involved and the mineral reactive surface area as follows (Lasaga et al., 1994):

$$r_m = k_m A_m \left[1 - \frac{Q_m}{K_m}\right] \qquad (5)$$

where k_m is the temperature-dependent kinetic rate constant [mol/(s m^2)], A_m is the specific reactive surface area of the mineral [m^2/(kg water)], Q_m is the ion activity product of the mineral and K_m is the equilibrium constant for the mineral-water interaction. The

temperature dependency of the mineral kinetic rate constant is described by the Arrhenius equation (Lasaga, 1984):

$$k_m = k_{25} exp\left[-\frac{E_a}{R}\left(\frac{1}{T}-\frac{1}{298.15}\right)\right] \qquad (6)$$

where R is the gas constant, equal to 8.314 J/(mol K), T is absolute temperature [K], E_a is the activation energy [J/mol] of the mineral and k_{25} is the rate constant [mol/(s m^2)] of mineral at 25°C. The parameters and initial value of variables used in equations (4) through (6) for mineral calcite are presented in Table 3.

Table 3. Parameters and initial values of variables used in equations (4)-(6) for mineral calcite.

k_{25}* [mol/(s m^2)]	E_a* [KJ/mol]	A_m** [m^2/(kg water)]	$c_{m,bulk}$** [mol/(m^3 bulk volume)]
1.60×10-9	41.87	38.68	6912.5

* From Svensson & Dreybrodt, 1992; **Initial values are calculated from initial volume fraction (corresponding to initial caprock porosity of 0.12) of minerals in porous rock matrix. The minerals reactive surface area is taken equal to 10% of the calculated physical surface area of the respective minerals.

2.4.5. Activity coefficients of aqueous species

The participation of aqueous species in the geochemical reactions is considered in the form of their effective concentration or activity (a) rather than their concentration to account for non-ideality of the aqueous solution (Langmuir, 1997; Betheke, 2008). The activity (dimensionless quantity) of aqueous species is related to their concentration (c_i) and the activity coefficient (γ_i) by the following relation (Lide et al., 2010):

$$a_i = \gamma_i \frac{c_i}{c_0} \qquad (7)$$

where c_0 is the standard concentration [1 mol/(kg water)]. The species activity coefficient is found as a function of species concentrations in the solution. The model presented by Duan & Sun, 2003 is used to calculate the activity coefficient of CO_{2aq}. The activity coefficients of electrically charged species are calculated using the extended Debye-Hückel function (B-dot equation). The B-dot equation is valid for NaCl dominant solutions up to ionic strength of 3

molal and for temperature conditions ranging from 0°C to 300°C (Betheke, 2008). The activity coefficients of electrically neutral species are calculated using the relations presented by Betheke, 2008(Appendix B).

2.4.6. Mineral reactive surface area

Minerals kinetic reactions cause variations in the corresponding reactive surface areas (A_m). In this study, the geometric approach is adopted for the calculation of minerals reactive surface (Johnson et al., 2004; Marini, 2007). The variations in A_m are modeled using the following relationship developed in this study:

$$A_m = 0.1\left(\frac{A_g}{\theta \rho_b V_g}\right)\left(MV c_{m,bulk}\right) \qquad (8)$$

where A_g, V_g, represents the physical surface area and volume of a mineral grain respectively assuming a spherical grain with a radius of 1.65×10^{-5} m; MV is the molar volume of mineral; $c_{m,bulk}$ is the mass of mineral updated in space and time through equation (4). The factor 0.1 shows the fraction of the mineral's reactive surface area to its geometrical surface area (Johnson et al., 2004). Equation (8) also accounts for the effects of fluid density.

2.4.7. Medium porosity

Minerals dissolution or precipitation change volume fractions (through equation 4) which in turn cause spatial and temporal variations in porosity. These are modeled as a function of variations in volume fractions of the minerals in the porous media:

$$\theta = 1 - VF_{rock,p} \qquad (9)$$

where $VF_{rock,p} = \sum_{m=1}^{n} VF_{m,p}$ is the sum of the volume fractions of all the minerals composing the porous rock; $VF_{m,p} = V_{m,p}/V_{rock,p}$ [m^3/m^3] is the volume fraction of the mineral, expressed as the ratio of the mineral volume to the total volume of the porous media. Some numerical restrictions are applied (Xu et al., 2014): (1) none of the

minerals are allowed to completely dissolve and disappear from the transport domain by setting a minimum threshold concentration value of 1×10^{-7} [mol/(m^3 bulk volume)]; (2) medium porosity is not allowed to fall below 1×10^{-3} by limiting further mineral precipitation.

2.4.8. Dispersion and diffusion of mobile species

The longitudinal dispersion in the fracture is defined by the Taylor-Aris dispersion formula as follows (e.g., Bodin et al., 2003):

$$D_D = D_L = \frac{2}{105}\mathbf{v^2}W_f^2\mathbf{D_b^{-1}} \qquad (12)$$

where $\mathbf{v}$ is the vertical fluid velocity in the fracture and $\mathbf{D_b}$ is the diagonal matrix of the molecular diffusion coefficient of the component species. At a constant temperature, the values of $\mathbf{D_b}$ are calculated from the diffusion coefficient of CO_{2aq} in water as follows (Al-Rawajfeh, 2004; Hassanzadeh et al., 2008):

$$\mathbf{D_b} = 10^{-0.87\log\left(\frac{\mu_b}{\mu_0}\right)}D_0\mathbf{I} \qquad (13)$$

where $\mathbf{I}$ is the identity tensor, and μ_0 and μ_b are the viscosities of water and brine, respectively. The viscosity of the brine is calculated from the model presented by Mao & Duan, 2009 (Appendix C). The diffusion coefficient of CO_{2aq} in pure water is calculated from the following relationship (Hassanzadeh et al., 2008):

$$D_0 = 10^{-4.1764+\frac{712.52}{T}-\frac{2.591\times10^5}{T^2}} \qquad (14)$$

The calculated values of μ_0, μ_b, D_0, and D_b for a 0.5 M NaCl solution and at various temperature and pressure values are presented in Table 4. The diffusion coefficients for all component species are taken equal to the calculated value of the diffusion coefficient of CO_{2aq} (Gherardi et al., 2007).

Table 4. Calculated values of viscosities and molecular diffusion coefficients at various pressure and temperature conditions.

Pressure and Temperature	μ_0 [Pa s]	μ_b[Pa s]	D_0 [m^2/s]	D_b[m^2/s]
105 bar and 45℃	5.96×10^{-4}	6.27×10^{-4}	3.19×10^{-9}	3.05×10^{-9}
155 bar and 60℃	4.69×10^{-4}	4.94×10^{-4}	4.25×10^{-9}	4.05×10^{-9}

2.4.9. Sorption of mobile species on the rock medium surfaces

The diagonal matrix of sorption partition coefficients ($\mathbf{K_d}$) used in equation (3) can be defined from the equilibrium sorption reaction (Bodin et al., 2003; Bear & Cheng, 2010):

$$[\mathbf{K_d}]_{i,i} = \left.\frac{[c_i]_s}{[c_i]_{aq}}\right|_{eq} \qquad (15)$$

where $[c_i]_s$ is the species concentration adsorbed on the solid (immobile) phase, expressed as the species concentration per unit mass of the solid [mol/kg] phase, and $[c_i]_{aq}$ is the concentration of the solute (mobile) in the fluid phase [mol/m^3]. However in this study the sorption process is modeled using a constant value of partition coefficient (K_d) taken equal to $2.5x10^{-4}$ m^3/kg for all the component species in the base-case transport scenarios.

Various minerals have shown to adsorb CO_{2aq} (Santschi & Rossi, 2006; Tabrizy et al., 2013). Santschi & Rossi, 2006 found that the adsorption of CO_2 on calcite surfaces depends on the adsorbed H_2O. Furthermore, these authors suggest that the adsorption of CO_2 on calcite surfaces results from specific interaction with a bifunctional surface intermediate ($Ca(OH)(HCO_3)$), which serves as a site for CO_2 adsorption. Their study shows that calcite has specific adsorption sites that accommodate additional CO_2 quantities beyond their regular aqueous dissolution process that were accounted for in this study. The partitioning coefficient from the slope of Figure 2(b) presented in Santschi & Rossi, 2006 is deduced as 6.6×10^{-2} m^3/kg. Fujii et al., 2010 conducted an experimental study of the sorption characteristics of CO_2 on rocks and minerals at pressure and temperature conditions that were relevant for the geological storage of CO_2. These authors observed the reversible nature of the CO_2 sorption

process. In their experimental studies, Heller & Zoback, 2014 reported the adsorption of CO_2 on various clay mineral samples under different pressure conditions. The authors found that the clay type "Eagle Ford 127", which mainly consists of calcite (80%), had the lowest capacity for CO_2 adsorption relative to the other clay samples. Table 5 presents the deduced values of sorption partition coefficient for various clay samples from study of Heller & Zoback, 2014 calculated from equation (6) and the values given in Table 2 of their study.

Table 5. Values of sorption partition coefficient K_d [m^3/kg] deduced from Heller & Zoback, 2014.

Clay sample	Barnett 31	Marcellus	Montney	Eagle Ford 127
Calcite content (%)	0	1	8.1	80
Clay content (%)	37.4	52	24.1	5
K_d [m^3/kg] value at 10.5 MPa	3.18×10^{-3}	1.54×10^{-3}	3.33×10^{-3}	7.39×10^{-4}
K_d [m^3/kg] value at 15.5 MPa	3.45×10^{-3}	1.62×10^{-3}	3.60×10^{-3}	7.93×10^{-4}

The values of sorption partition coefficient used in this study ($7.50\ x10^{-4}$, $2.50\ x10^{-4}$, and $8.33x10^{-5}$ m^3/kg) are much lower than the values reported by Santschi & Rossi, 2006 and Heller & Zoback, 2014. These authors used crushed rock, which has a higher reactive surface area, rather than intact rock.

2.4.10. Initial and boundary conditions

The initial and boundary conditions associated with the transport system formed by equations (2) and (3) for the fracture and the rock matrix are presented as follows:

Initial conditions in the transport domain:

$$\mathbf{u_i}(x, y, t) = \mathbf{u_{i,0}} \qquad (16)$$

Inflow (bottom of the fracture and the matrix):

$$\mathbf{u_i}(y = 0, t) = \mathbf{u_{i,bc}} \qquad (17)$$

No flux (line of symmetry assumed at center of the fracture):

$$-\mathbf{n} \cdot [(\mathbf{D_D} + \mathbf{D_e})\nabla\mathbf{u} + \mathbf{vu}] = 0 \quad \text{for } x = 0 \qquad (18)$$

No flux (line of symmetry assumed at right sided boundary of the rock matrix):

$$-\mathbf{n}\cdot[(\mathbf{D_D}+\mathbf{D_e})\nabla\mathbf{u}+\mathbf{vu}]=0 \qquad \text{for } x=W_f+W_m \qquad (19)$$

Outflow (top boundaries of the fracture and the rock matrix):

$$-\mathbf{n}\cdot[(\mathbf{D_D}+\mathbf{D_e})\nabla\mathbf{u}]=0 \qquad \text{for } y=L \qquad (20)$$

where $\mathbf{n}$ is a unit normal vector that is perpendicular to the boundary surface. This system is completed by the continuity condition at the fracture-matrix interface boundary. The outflow boundary condition assumes that the transport of species is only caused by advection. For a zero fluid velocity in the rock matrix, the top of the rock matrix acts as a no flow boundary. The inflow boundary conditions (constant fluid velocity in the fracture and constant species concentration) are adopted as a basis for generic process analyses. A constant vertical velocity is assumed to prevail in the fracture during the entire simulation time. The initial and boundary conditions written in terms of component species are presented in Table 6.

Table 6. Initial (sub-index 0) and boundary conditions (sub-index bc).

Pressure and temperature	45°C and 105 bar	60°C and 155 bar
Component species	Concentration [mol/(kg water)]	Concentration [mol/(kg water)]
$u_{HCO_{3,0}}$	4.02×10^{-3}	3.10×10^{-3}
u_{Na_0}	5.00×10^{-1}	5.00×10^{-1}
u_{Ca_0}	2.01×10^{-3}	1.55×10^{-3}
$u_{CO_{2,0}}$	1.82×10^{-4}	1.38×10^{-4}
$u_{HCO_{3,bc}}$	7.17×10^{-2}	5.95×10^{-2}
$u_{Na_{bc}}$	5.00×10^{-1}	5.00×10^{-1}
$u_{Ca_{bc}}$	3.58×10^{-2}	2.97×10^{-2}
$u_{CO_{2,bc}}$	1.08	1.06

2.4.11. Various base-case transport scenarios

Various base-case transport scenarios are analyzed for a period of 500 years (Table 7). Mass transport without any geochemical reactions is analyzed in mass transport scenarios 1, 2 and 3 whereas the reactive transport is performed in reactive transport scenarios 4 and 5. These base-case transport scenarios are performed for P and T values of 105 bar and 45°C respectively. In these base-case transport scenarios, a constant fluid vertical velocity of 3.171×10^{-7} m/s (10 m/year) is used in the fracture.

Table 7. Various base-case transport scenarios.

Scenarios	Processes accounted for
1	No interaction between fracture and matrix
2	Molecular diffusion between fracture and matrix, no calcite mineral reaction in the matrix, no sorption in the matrix
3	Molecular diffusion between fracture and matrix, no calcite mineral reaction in the matrix, sorption in the matrix
4	Molecular diffusion between fracture and matrix, calcite mineral reaction in the matrix, no sorption in the matrix
5	Molecular diffusion between fracture and matrix, calcite mineral reaction in the matrix, sorption in the matrix

2.4.12. Sensitivity analysis

Sensitivity analysis is performed to analyze the effects of different fluid vertical velocities (v) in the fracture, the sorption partition coefficient (K_d), P and T values and the diffusion coefficient on the mass uptake of CO_{2aq} in geochemical reactions. Two sets of P and T values are considered; 105 bar and 45°C and 155 bar and 60°C, which are thought to represent reservoir depths of 1040 m and 1540 m below the land surface respectively. For the sensitivity analysis, the base-case transport scenarios 3 and 5 are further divided into sub-scenarios for different velocities in the fracture, sorption partitioning coefficients, P and T values and diffusion coefficient (Table 8). These scenarios 3 and 5 represent all the considered transport processes (diffusion in the matrix, sorption on the rock surfaces in the matrix and mineral kinetic reactions). Moreover, in the sensitivity analysis, the number of

mass transport scenarios (3.1, 3.2, 3.3, 3.4, 3a and 3b) equaled the number of reactive transport scenarios (5.1, 5.2, 5.3, 5.4, 5a and 5b).

Table 8. Sensitivity analysis for various parameters using the base-case transport scenarios 3 and 5.

Sub-scenarios	Velocity in the fracture, v [m/s]	Distribution coefficient, K_d [m^3/kg]	Pressure and temperature	Diffusion coefficient [m^2/s]
3.1	$3.17x10^{-8}$	$2.50x10^{-4}$	105 bar and 45°C	3.05×10^{-9}
3.2	$6.34x10^{-7}$	$2.50x10^{-4}$	105 bar and 45°C	3.05×10^{-9}
3.3	$3.17x10^{-7}$	$7.50x10^{-4}$	105 bar and 45°C	3.05×10^{-9}
3.4	$3.17x10^{-7}$	$8.33x10^{-5}$	105 bar and 45°C	3.05×10^{-9}
5.1	$3.17x10^{-8}$	$2.50x10^{-4}$	105 bar and 45°C	3.05×10^{-9}
5.2	$6.34x10^{-7}$	$2.50x10^{-4}$	105 bar and 45°C	3.05×10^{-9}
5.3	$3.17x10^{-7}$	$7.50x10^{-4}$	105 bar and 45°C	3.05×10^{-9}
5.4	$3.17x10^{-7}$	$8.33x10^{-5}$	105 bar and 45°C	3.05×10^{-9}
3a	$3.17x10^{-7}$	$2.50x10^{-4}$	155 bar and 60°C	3.05×10^{-9}
5a	$3.17x10^{-7}$	$2.50x10^{-4}$	155 bar and 60°C	3.05×10^{-9}
3b	$3.17x10^{-7}$	$2.50x10^{-4}$	155 bar and 60°C	4.05×10^{-9}
5b	$3.17x10^{-7}$	$2.50x10^{-4}$	155 bar and 60°C	4.05×10^{-9}

2.4.13. Calculation of mass uptake of CO_{2aq} in geochemical reactions

The mass of CO_{2aq} consumed in the geochemical reactions in each reactive transport scenario (scenarios 4, 5, 5.1, 5.2, 5.3, 5.4, 5a, and 5b) is calculated by comparing the CO_{2aq} mass balances with the corresponding mass transport scenario (scenarios 2, 3, 3.1, 3.2, 3.3, 3.4, 3a and 3b) for better accuracy. The mass uptake of CO_{2aq} in geochemical reactions is calculated by mass balance considerations involving the cumulative mass entering and exiting through the inflow and outflow boundaries, and that stored in the aqueous and adsorbed states within the domain. In order to estimate the quantities of CO_{2aq} mass uptake in geochemical reactions in relation to the mass inflow through the bottom inflow boundaries in each reactive transport scenario, the mass uptake quantities are presented in terms of normalized mass uptake. The normalized mass uptake of CO_{2aq} ($\boldsymbol{m_{con}^{n}} = \frac{\boldsymbol{m_{con}}}{\boldsymbol{m_{in}}}$) is the cumulative mass consumed ($\boldsymbol{m_{con}}$) normalized with respect to the cumulative mass that entered the domain through the bottom inflow boundaries ($\boldsymbol{m_{in}}$) over the period of time.

3. Results

3.1. Background brine composition in the reservoir and the transport domain

From the background BGM, the solution was found equilibrated at a pH of 7.26 and contains Na^+ and Cl^- as the two major species representing the effects of brine, followed by HCO_3^-, Ca^{2+}, $NaHCO_{3aq}$, and CO_{2aq} as the intermediate species that characterize the brine-rock equilibrium with respect to calcite. The remaining species were present at trace levels (Table 9).

Table 9. Species concentrations from the background BGM at 45°C and 0.01 bar (column 2) and from CO_{2g} dissolution reaction modeling performed at 45°C and 105 bar (column 3).

Pressure and temperature	45°C and 0.01 bar	45°C and 105 bar
Species	c [mol/(kg water)]	c [mol/(kg water)]
HCO_3^-	3.33×10^{-3}	6.04×10^{-2}
Na^+	4.99×10^{-1}	4.89×10^{-1}
Cl^-	5.00×10^{-1}	5.00×10^{-1}
Ca^{2+}	2.01×10^{-3}	3.58×10^{-2}
CO_{2aq}	1.98×10^{-4}	1.08
H^+	5.44×10^{-8}	1.67×10^{-5}
OH^-	1.29×10^{-6}	4.25×10^{-9}
CO_3^{2-}	1.43×10^{-5}	8.85×10^{-7}
$NaHCO_{3aq}$	6.63×10^{-4}	1.13×10^{-2}

3.2. Solubility of CO_{2g} and the resulting brine composition in the reservoir

Due to the dissolution of CO_{2g}, the concentration of CO_{2aq} in the 0.5 M NaCl brine stabilized at approximately 1.08 mol/(kg water), at a temperature of 45°C and pressure of 105 bar (see Table 9). An increase in the concentration of CO_{2aq} resulted in a drop in pH from 7.26 to 4.78.

3.3. Reactive transport

Initially, the dissolved species in the pore water in the transport domain of fracture-matrix system were at chemical equilibrium and saturated with respect to the calcite mineral. The mixing of leaking CO_2-saturated brine, also saturated with respect to calcite, with the parent pore water in the transport domain disturbed the chemical equilibrium and turned the

geochemical conditions to undersaturation with respect to calcite in close vicinity of the bottom inflow boundaries. This initiated the calcite reaction in the rock matrix. In the rock matrix, calcite was allowed to dissolve or precipitate depending on the saturation state over the period of time.

3.3.1. Base-case transport scenarios

Figure 2 shows the saturation state with respect to calcite at onset (1 second(s)) of the simulation for scenario-4 (without sorption) and scenario-5 (with sorption) caused by mixing of leaking CO_2-saturated brine with the resident water. The observed lower values of saturation with respect to calcite were 0.09 and 0.04 in scenarios 4 and 5 respectively.

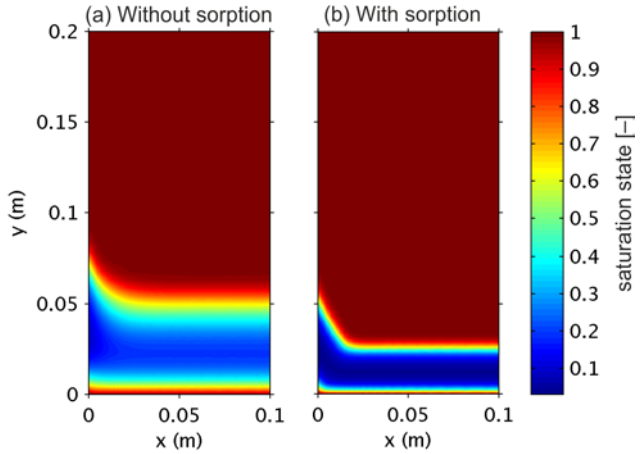

Figure 2. Saturation state of calcite at onset (1 s) of the simulation for (a); scenario-4 (without sorption); and (b) scenario-5 (with sorption).

The decrease in saturation state with respect to calcite below unity initiated the calcite dissolution reaction near the bottom (inflow) boundary in the rock matrix. Figure 3 shows the calcite reaction rate for scenario-4 (no sorption) and scenario-5 (with sorption) at onset (1 s) of the simulation. The difference in spread of reaction zones between Figures 3a and 3b is due to the sorption that has constrained the transport of species in scenario-5. It can also be observed that sorption causes relatively larger calcite kinetic reactions (either dissolution or precipitation).

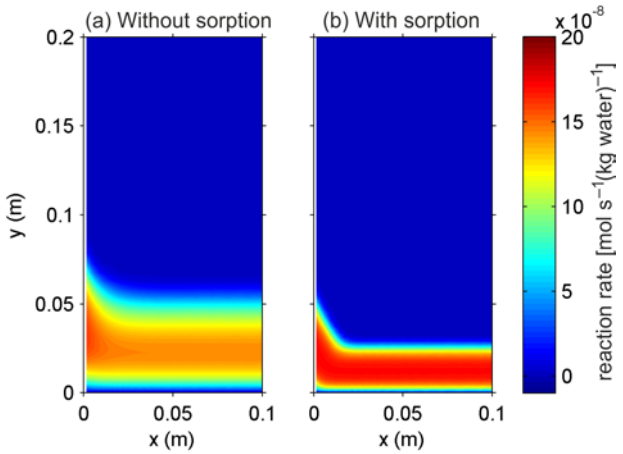

581

582 **Figure 3**. Calcite reaction rate [mol/(s kg water)] at onset (1 s) of the simulation for; (a)
583 scenario-4 (without sorption); and (b) scenario-5 (with sorption).
584

585 The calcite dissolution reaction in the rock matrix driven by higher concentration of CO_{2aq} in
586 the leaking brine caused the production of Ca^{2+} and HCO_3^- species (Kaufmann & Dreybrodt,
587 2007). The conversion of CO_{2aq} in the calcite dissolution reaction has spatially constrained
588 the corresponding concentration plume relative to the other species (Ca^{2+} and HCO_3^-) due to
589 their production in calcite dissolution reaction. Figure 4 shows the concentration plumes of
590 CO_{2aq}, Ca^{2+} and HCO_3^- for scenario-5 (with sorption) after 500 years.

591

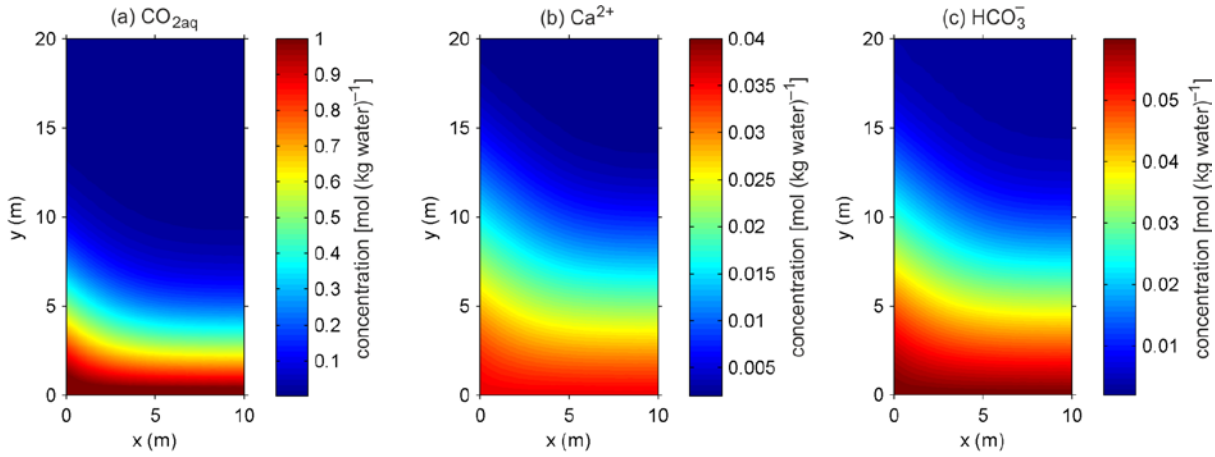

592
593
594 **Figure 4**. Spatial distribution of the concentrations [mol/(kg water)] of dissolved species after
595 500 years for scenario-5; (a) CO_{2aq}; (b) Ca^{2+}; and (c) HCO_3^{-1}.
596

Over time, calcite reaction in the rock matrix resulted in variations in the mass of calcite with associated changes in the mineral reactive surface area. Figure 5a and 5b shows these variations for scenario-5 after 500 years.

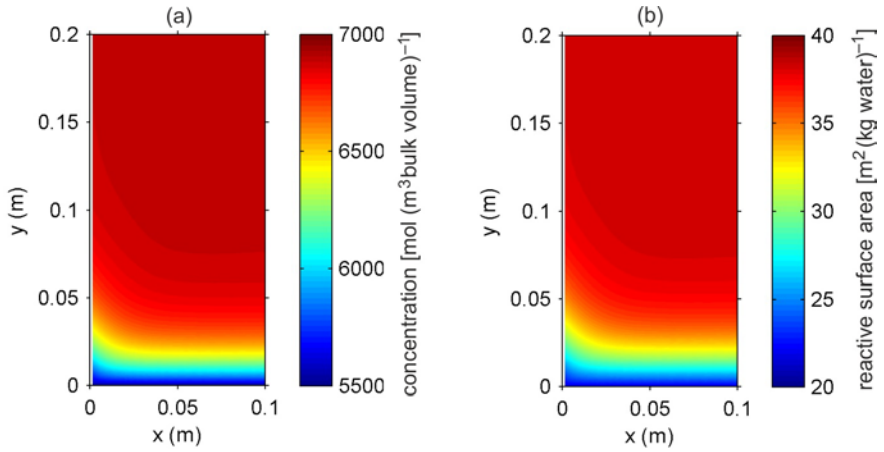

Figure 5. Effects of the calcite reaction on the; (a) mass of calcite [mol/(m^3 bulk volume)] for scenario-5; (b) calcite reactive surface area [m^2/(kg water)] for scenario-5 after 500 years.

Variations in porosity (Figure 6a) and medium permeability (Figure 6b) as well as effective diffusivity of dissolved species in the rock matrix (Figure 6c) for scenario-5 are also presented. These variations have been observed mainly close to the bottom inflow boundary.

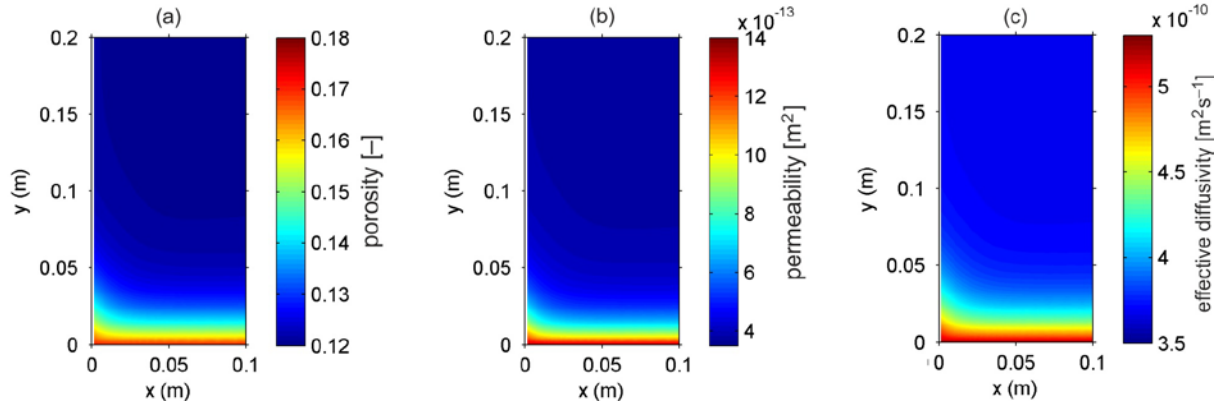

Figure 6. Effects of the calcite reaction on (a) medium porosity for scenario-5; (b) medium permeability [m^2] for scenario-5; (c) effective diffusivity [m^2/s] for scenario-5 after 500 years.

Initially, the pore water in the fracture-matrix system had a pH of 7.26, while that in the CO_2-injected reservoir was 4.78. Apart from mixing, pH was affected by both sorption and calcite kinetic reaction in the rock matrix. Figure 7 shows how the pH in the fracture-matrix transport domain evolves after 500 years for various transport scenarios. In the absence of calcite reaction, the low pH spreads farther in scenario-2 (no sorption, Figure 7a) than in the scenario-3 (with sorption, Figure 7b). The calcite kinetic reaction retards the transport of low pH brine for scenario-4 (no sorption, Figure 7c) and scenario-5 (with sorption, Figure 7d). The higher pH values observed in the reactive transport scenarios (4, 5) as compared to mass transport scenarios (2, 3) are due to consumption of H^+ in the calcite dissolution reaction.

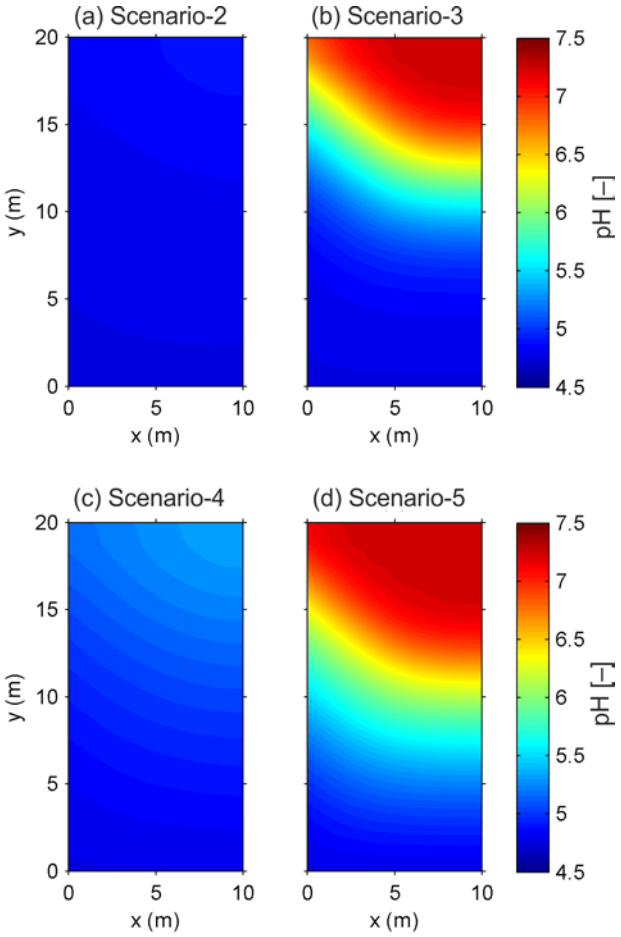

Figure 7. Evolution of pH in the fracture-matrix system after 500 years for various base-case transport scenarios; (a) scenario-2 (no calcite reaction, no sorption); (b) scenario-3 (no calcite reaction with sorption); (c) scenario-4 (calcite reaction, no sorption); and (d) scenario-5 (calcite reaction with sorption).

Figure 8 shows the normalized mass uptake of CO_{2aq} in percentage due to geochemical reactions (aqueous phase equilibrium and calcite kinetic reactions) for the (i) no sorption and (ii) sorption cases. After 500 years, the normalized mass uptake of CO_{2aq} declined to 4.43% for the no sorption case whereas it was 4.97% when sorption was included in the analysis. Although higher mass uptake of CO_{2aq} resulted in scenario-5 compared to scenario-4 (Table 10), the observed lower value of normalized mass uptake of CO_{2aq} in the former scenario compared to the latter has been mainly due to the normalization of the mass uptake with respect to the mass inflow through the bottom inflow boundaries in the respective scenario. At the initial times of the simulation, sorption causes relatively higher concentration gradients across the inflow boundaries in scenario-5 compared to those in scenario-4. Sorption process fixes species' mass in adsorbed state on the rock surfaces and reduces species' mass in aqueous state which in turn causes higher concentration gradients across the bottom inflow boundaries.

Over the period of time, relatively lower saturation state with respect to calcite prevailed in the rock matrix in scenario-5 compared to that in scenario-4. The sorption process caused a relatively lower concentration of Ca^{2+} and HCO_3^{-1} in the aqueous state in scenario-5 compared to scenario-4 that resulted in lower saturation state of calcite in the former scenario than the latter. The resulting lower saturation state of calcite caused relatively higher calcite dissolution reaction thus contributing towards higher mass uptake of CO_{2aq} in geochemical reactions in scenario-5 compared to that in scenario-4. Prevailing higher mass uptake relative to mass inflow in scenario-5 resulted in higher normalized mass uptake in scnario-5 compared to scenario-4 in the later times of the simulation. Lower mass uptake relative to mass inflow in scenario-4 resulted in lower normalized mass uptake in this

scenario than that in scenario-5 after nearly 277 years.

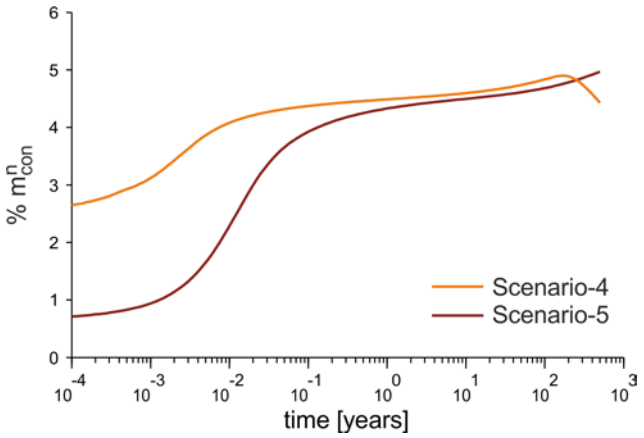

Figure 8. The percent normalized uptake of CO_{2aq} in geochemical reactions without sorption (scenario-4) and with sorption (scenario-5).

Table 10 presents the mass balance of CO_{2aq} in the base-case reactive transport scenarios 4 and 5 after 500 years of simulation time. A total of 6.26×10^{2} [mol] and 1.45×10^{3} [mol] of CO_{2aq} have been consumed in geochemical reactions over the period of 500 years in scenario-4 and scenario-5 respectively. Thus sorption in scenario-5 has caused CO_{2aq} mass conversion (through geochemical reactions) approximately twice that observed without sorption in scenario-4. This result is consistent with the increase in total pore volume resulting from calcite dissolution in the rock matrix domain which was observed almost double in scenario-5 compared to scenario-4 (see Table 12). For the same fluid velocity in the fracture, higher total mass uptake of CO_{2aq} in scenario-5 compared to scenario-4 is (i) mainly due to higher mass inflow through the bottom inflow boundaries in scenario-5 driven by sorption process, and (ii) to a lesser extent to relatively lower saturation state of calcite caused by sorption in scenario-5 compared to scenario-4. Higher total mass inflow in scenario-5 compared to that in scenario-4 resulted in overall higher calcite dissolution and higher total mass uptake of CO_{2aq} in former scenario compared to the

latter. In Table 10 we can also observe that the mass of CO_{2aq} is conserved, with mass balance errors lower than 0.10%.

Table 10. Mass [mol] balance of CO_{2aq} in the base-case reactive transport scenarios 4 and 5.

Scenarios	Scenario-4	Scenario-5
Total mass entered the domain	1.41×10^{4}	2.91×10^{4}
Mass entered the domain due to advection	5.39×10^{3}	5.39×10^{3}
Mass entered the domain due to diffusion	8.73×10^{3}	2.37×10^{4}
Mass entered the domain due to dispersion	9.15×10^{-5}	2.96×10^{-4}
Mass left the domain	4.27×10^{2}	9.63×10^{-1}
Mass stored in aqueous state	1.31×10^{4}	4.68×10^{3}
Mass stored in adsorbed state	0	2.30×10^{4}
Mass consumed in geochemical reactions	6.26×10^{2}	1.45×10^{3}
% normalized mass uptake of CO_{2aq} after 500 years	4.43	4.97
% error in mass balance	6.00×10^{-2}	7.33×10^{-2}

Due to the small width of the fracture (1 mm) compared to that of the rock matrix (10 m), and low advective velocity in the fracture, the total mass inflow (by advection, dispersion and diffusion) through the bottom inflow boundary of the fracture is small compared to that entering (by diffusion) through the bottom inflow boundary of the rock matrix. Table 11 presents the division of total mass entered the domain through the bottom inflow boundaries of fracture and matrix in reactive transport scenarios 4 and 5 for simulation time of 500 years.

Table 11. Mass [mol] of CO_{2aq} that entered the domain through bottom inflow boundaries of fracture and rock matrix in the reactive transport scenarios 4 and 5.

Scenarios	Scenario-4		Scenario-5	
Bottom inflow boundary	fracture	matrix	fracture	matrix
Total mass entered the domain	5.39×10^{3}	8.73×10^{3}	5.39×10^{3}	2.37×10^{4}
Mass entered the domain due to advection	5.39×10^{3}	0	5.39×10^{3}	0
Mass entered the domain due to diffusion	4.46×10^{-1}	8.73×10^{3}	1.44×10^{0}	2.37×10^{4}
Mass entered the domain due to dispersion	9.15×10^{-5}	0	2.96×10^{-4}	0

690 Table 12 presents the mass balance of Ca^{2+} and calcite (mineral) for the reactive transport
691 scenarios 4 and 5 after 500 years. It can be observed that the mass [mol] of Ca^{2+} produced is
692 equal (except numerical errors of less than 0.5%) to the mass of calcite dissolved from the
693 kinetic reaction. Table 12 also presents the values of increase in total pore volume [m^3] due to
694 calcite dissolution in the rock matrix. An increase in the total pore volume of the rock matrix
695 is found due to higher calcite dissolution than its precipitation. It is found that in the reactive
696 transport scenarios 4 and 5 the pore volume reached values of 24.023 m^3 and 24.052 m^3
697 respectively from the initial value of 24 m^3.

698 **Table 12**. Mass [mol] balance of Ca^{2+}, mineral calcite and total pore volume of rock matrix in
699 the base-case reactive transport scenarios 4 and 5 after 500 years.

Scenarios	Scenario-4	Scenario-5
Mass [mol] of Ca^{2+} produced in dissolution of mineral calcite	6.22×10^{2}	1.41×10^{3}
Mass [mol] of mineral calcite dissolved	6.25×10^{2}	1.41×10^{3}
Increase in pore volume [m^3]	2.31×10^{-2}	5.21×10^{-2}
% error in mass balance	4.89×10^{-1}	2.35×10^{-1}

700

701 The retardation in transport of transported species along the fracture was analyzed in terms of
702 breakthrough curves representing the concentration of dissolved species at specified locations
703 along the fracture. Figure 9 presents the breakthrough curve of CO_{2aq} at the top (outflow)
704 boundary of the fracture for scenario-1, corresponding to no mass interaction between the
705 species in the fracture and those in the adjacent rock matrix. An observable increase in
706 concentration of CO_{2aq} at the outflow boundary of the fracture becomes visible only after 1.25
707 years. We observe that the concentration of CO_{2aq} at the outflow boundary has attained the
708 value equal to the one applied at the inflow boundary after only 2.8 years.

709

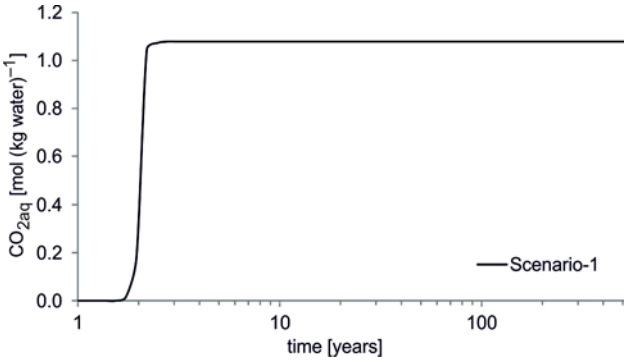

710

711

712 **Figure 9**. Breakthrough curve for the base-case transport scenario-1 showing the
713 concentration of CO_{2aq} at top outflow of the fracture over the period of time.
714

715 Figure 10 presents the breakthrough curves for CO_{2aq}, for various base-case transport
716 scenarios 2 through 5, at 10 m (mid-way of the fracture) and 20 m (top outflow boundary of
717 the fracture). An observable increase in concentration of CO_{2aq} at 10 m and 20 m locations
718 along the fracture becomes visible only after nearly 16 and 50 years, respectively. Comparing
719 the breakthrough curves for scenario-1 (Figure 9) and scenario-2 (Figure 10a), it can be
720 observed that the mass exchange between the conducting fracture and the adjacent rock
721 matrix has caused significant retardation in the transport of CO_{2aq} in scenario-2. We can
722 further see that sorption has also caused a significant retardation in the transport of CO_{2aq}
723 (scenario-2 Vs scenario-3 and scenario-4 Vs scenario-5). Due to significant retardation caused
724 by sorption, the concentration of CO_{2aq} does not increase, within the simulation period, to a
725 level that would make it visible at top outflow boundary of the fracture in scenarios 3 and 5
726 (Figure 10b). Mass uptake of CO_{2aq} in geochemical reactions has also caused transport
727 retardation. However, compared to sorption, the mass uptake of CO_{2aq} in geochemical
728 reactions has caused relatively small retardation in its transport (scenario-2 Vs scenario-4 and
729 scenario-3 Vs scenario-5).

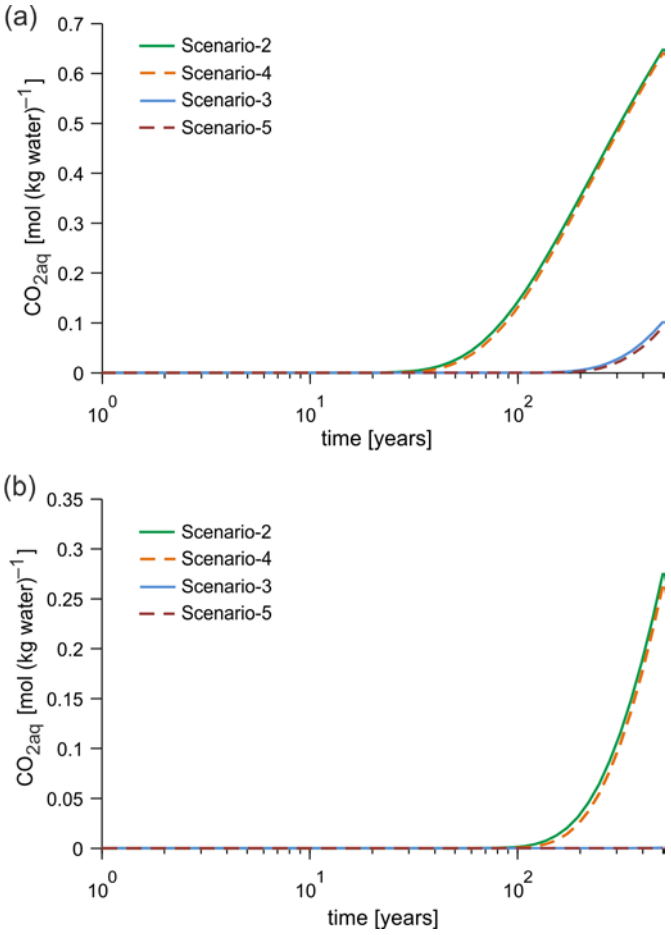

730

731

732 **Figure 10**. Breakthrough curves showing the concentration of CO_{2aq} for various base-case
733 transport scenarios along the fracture, at; (a) 10 m from the inflow boundary; and (b) 20 m
734 from the inflow boundary.
735

736 *3.3.2. Sensitivity analysis*

737 *3.3.2.1. Role of fluid velocity in fracture and sorption partition coefficient*

738 Figure 11 shows the normalized mass uptake of CO_{2aq} in geochemical reactions in the
739 reactive transport scenarios (5.1, 5.2, 5.3, and 5.4) studied in the sensitivity analysis.
740 For the same sorption partition coefficient, it can be observed in Figure 11(a) that the
741 normalized mass uptake of CO_{2aq} decreased as the vertical velocity in the fracture increased
742 (scenario-5.1 Vs scenario-5.2). On the other hand in Figure 11(b), for the same fluid velocity
743 in the fracture, the normalized mass uptake decreased with increase in sorption partition
744 coefficient (scenario-5.4 Vs scenario-5 and scenario-5.3).

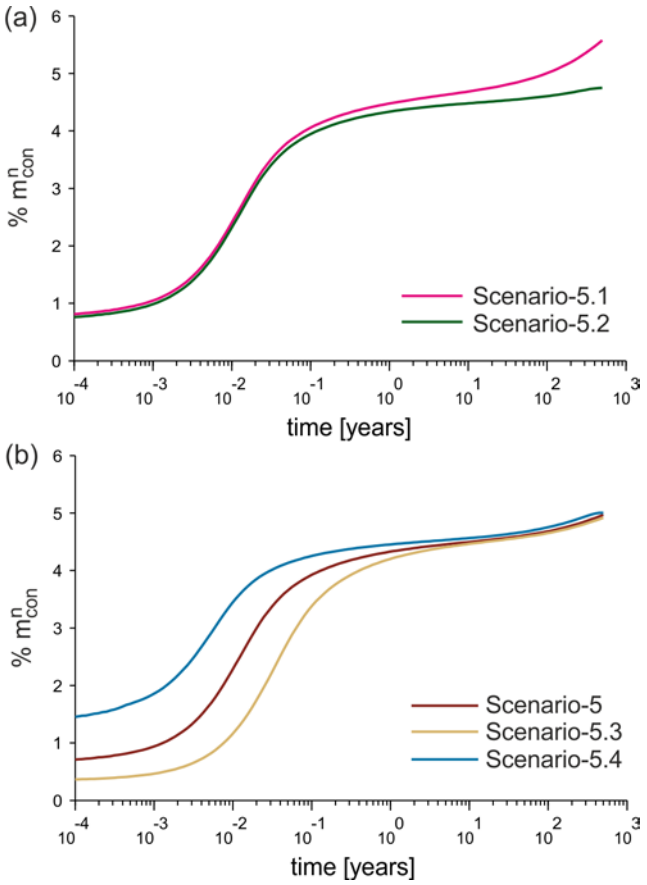

Figure 11. The percent normalized uptake of CO_{2aq} in geochemical reactions for various reactive transport scenarios; (a) scenarios 5.1 and 5.2; (b) scenarios 5, 5.3, and 5.4.

To elaborate the graphical results presented in Figure 11 we have also calculated the overall mass balance of CO_{2aq} in the transport domain for the reactive transport scenarios 5.1 through 5.4 (Table 13). In Table 13, higher mass uptake of CO_{2aq} can be observed in scenario-5.2 (1.60×10^{3} mol) compared to scenario-5.1 (1.41×10^{3} mol), however an opposite behaviour is observed in Figure 11(a). Higher fluid velocity in the fracture in scenario-5.2 results in higher advective mass inflow through the bottom inflow boundary of fracture. This caused a lower normalized CO_{2aq} mass uptake in scenario-5.2 compared to that in scenario-5.1. Also from Table 10 and Table 13, higher mass uptake of CO_{2aq} can be observed in scenario-5.3 (2.23×10^{3} mol) compared to

scenario-5 (1.45×10^{3} mol) and scenario-5.4 (1.03×10^{3} mol) but the opposite behaviour is observed in Figure 11(b). Lower sorption in scenario-5.4 causes lower diffusive mass inflow mainly through the bottom inflow boundary of rock matrix which results in higher normalized mass uptake in scenario-5.4 compared to scenarios 5 and 5.3. Thus the normalized mass uptake trends presented in Figure 11, showing the opposite of actual mass uptake (Table 13), are due to the normalization of the mass uptake with respect to mass the inflow through the bottom inflow boundaries.

Table 13. Mass [mol] balance of CO_{2aq} in various reactive transport scenarios (5.1, 5.2, 5.3, and 5.4) studied in the sensitivity analysis.

Scenarios	Scenario-5.1	Scenario-5.2	Scenario-5.3	Scenario-5.4
Total mass entered the domain	2.59×10^{4}	3.37×10^{4}	4.53×10^{4}	2.06×10^{4}
Mass entered the domain due to advection	5.39×10^{2}	1.08×10^{4}	5.39×10^{3}	5.39×10^{3}
Mass entered the domain due to diffusion	2.53×10^{4}	2.29×10^{4}	3.99×10^{4}	1.53×10^{4}
Mass entered the domain due to dispersion	2.96×10^{-5}	2.52×10^{-4}	5.87×10^{-4}	1.71×10^{-4}
Mass left the domain	9.11×10^{-2}	2.75×10^{1}	9.11×10^{-1}	1.85×10^{1}
Mass stored in aqueous state	4.13×10^{3}	5.42×10^{3}	2.77×10^{3}	7.41×10^{3}
Mass stored in adsorbed state	2.03×10^{4}	2.66×10^{4}	4.03×10^{4}	1.22×10^{4}
Mass converted in geochemical reactions	1.41×10^{3}	1.60×10^{3}	2.23×10^{3}	1.03×10^{3}
% normalized mass uptake of CO_2 after 500 years	5.46	4.75	4.91	5.00
% error in mass balance	8.27×10^{-2}	6.19×10^{-2}	7.63×10^{-2}	6.77×10^{-2}

Table 14 presents the mass balance of Ca^{2+} and calcite (mineral) for the reactive transport scenarios 5.1 through 5.4 after 500 years. It also presents an increase in total pore volume [m^3] which is well correlated with calcite dissolution in the rock matrix. It can also be observed that the difference between the mass of calcite dissolved and Ca^{2+} produced is lower than 0.36% in all these reactive transport scenarios.

775 **Table 14.** Mass [mol] balance of Ca^{2+}, mineral calcite and pore volume of rock matrix in
776 various reactive transport scenarios (5.1, 5.2, 5.3, and 5.4) studied in the sensitivity analysis.

Scenarios	Scenario-5.1	Scenario-5.2	Scenario-5.3	Scenario-5.4
Mass [mol] of Ca^{2+} produced in dissolution of mineral calcite	1.37×10^{3}	1.56×10^{3}	2.13×10^{3}	1.01×10^{3}
Mass [mol] of mineral calcite dissolved	1.37×10^{3}	1.57×10^{3}	2.14×10^{3}	1.02×10^{3}
Increase in pore volume [m^3]	5.07×10^{-2}	5.79×10^{-2}	7.90×10^{-2}	3.75×10^{-2}
% error in mass balance	2.46×10^{-1}	2.11×10^{-1}	2.42×10^{-1}	3.02×10^{-1}

777

778 *3.3.2.2. Role of temperature and diffusion coefficient*

779 In addition to the base-case transport scenarios 3 and 5, which were performed at 105 bar and
780 45°C, transport scenarios 3a, 3b, 5a, and 5b were also performed at 155 bar and 60°C to
781 analyze the effects of pressure and temperature and diffusion coefficient on the mass uptake
782 of CO_{2aq} in geochemical reactions. Due to changes in P and T values, the initial and the
783 boundary conditions required for transport modeling were also changed. These values were
784 obtained by performing an additional background BGM and CO_{2g} dissolution modeling for
785 these pressure and temperature conditions, and the results were presented in Table 6 (column
786 3). Results from CO_{2g} dissolution modeling showed that brine in the reservoir got saturated at
787 relatively lower concentration of CO_{2aq} with increase in temperature (Table 6).

788

789 Table 15 presents the mass balance of CO_{2aq} in reactive transport scenarios 5a and 5b. For the
790 same values of fluid velocity in the fracture, sorption partition coefficient and diffusion
791 coefficient in scenarios 5 and 5a, relatively lower mass inflow in the latter scenario (2.85×10^{4}
792 mol) compared to that in the former one (2.91×10^{4} mol) was due to lower concentration of
793 CO_{2aq} in leaking CO_2-saturated brine as a result of higher temperature in scenarios 5a and 5b
794 compared to rest of the scenarios. Lower mass uptake of CO_{2aq} in scenario-5a (1.29×10^{3}
795 mol) compared to that in scenario-5 (1.45×10^{3} mol) is (i) mainly due to lower calcite

kinetic reaction with increased temperature in scenario-5a and (ii) to a lesser extent due to lower mass inflow resulting from lower concentration of CO_{2aq} in the leaking brine in scenario-5a.

For the same values of velocity in the fracture, sorption partition coefficient and temperature in scenarios 5a and 5b, relatively higher mass inflow in the latter scenario (3.21×10^{4} mol) compared to that in the former one (2.85×10^{4}) resulted from higher diffusion coefficient used in scenario-5b than in scenario-5a. The higher mass inflow resulted in higher total mass uptake in scenario-5b (1.46×10^{3} mol) compared to that in scenario-5a (1.29×10^{3} mol). Also the negligible error in mass balance shows that the condition of mass conservation of CO_{2aq} is well satisfied by the numerical solution method.

Table 15. Mass [mol] balance of CO_{2aq} in reactive transport scenarios 5a, and 5b.

Scenarios	Scenario-5a	Scenario-5b
Total mass entered the domain	2.85×10^{4}	3.21×10^{4}
Mass entered the domain due to advection	5.29×10^{3}	5.29×10^{3}
Mass entered the domain due to diffusion	2.32×10^{4}	2.68×10^{4}
Mass entered the domain due to dispersion	2.85×10^{-4}	3.04×10^{-4}
Mass left the domain	7.44×10^{-1}	8.12×10^{-1}
Mass stored in aqueous state	4.60×10^{3}	5.18×10^{3}
Mass stored in adsorbed state	2.26×10^{4}	2.55×10^{4}
Mass converted in geochemical reactions	1.29×10^{3}	1.46×10^{3}
% normalized mass uptake of CO_2 after 500 years	4.529	4.534
% error in mass balance	7.36×10^{-2}	7.54×10^{-2}

Figure 12 presents the normalized mass uptake of CO_{2aq} in geochemical reactions in reactive transport scenarios 5, 5a, and 5b. Higher temperature in scenarios 5a and 5b has resulted in lower normalized mass uptake of CO_{2aq} in geochemical reactions in these scenarios (4.53%) as compared to scenario-5 (4.98%) after 500 years. On the other hand due to same temperature and thus the same calcite reaction kinetics, nearly the same normalized mass uptake of CO_{2aq} resulted in scenarios 5a and 5b.

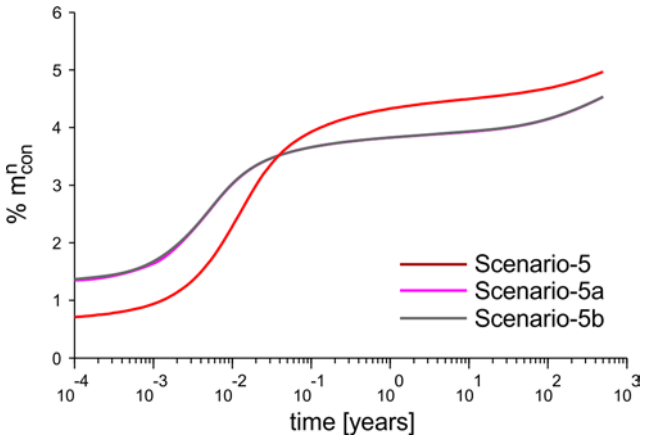

Figure 12. The percent normalized mass uptake of CO_{2aq} in geochemical reactions in reactive transport scenarios 5, 5a and 5b.

4. Discussion

Dissolution of CO_{2g} in the reservoir brine made the solution more acidic by decreasing its pH from 7.26 to 4.78. The decrease in pH depends on the CO_{2aq} concentration in the solution and on the type of minerals in contact with the solution. In the analyzed geochemical system, mineral calcite provided a buffer and maintained the pH at a value of 4.78, which is slightly greater than the pH that would be expected in the absence of mineral calcite (Hellevang, 2006; Pokrovsky et al., 2009).

According to the stoichiometry of the calcite reaction (R5), H^+ is consumed from the solution and Ca^{2+} and HCO_3^- are produced. The reaction of H^+ with calcite is associated with the conversion of CO_{2aq} to H^+ (Dreybrodt et al., 1996; Kaufmann & Dreybrodt, 2007). The dissolution of calcite results in the conversion of CO_{2aq} from the solution, whereas the precipitation of calcite may result in the release of CO_{2aq} in the solution (Dreybrodt et al., 1997). Over time, calcite has either dissolved or precipitated depending on the geochemical conditions in the transport domain. However, the observed higher dissolution of calcite relative to its precipitation in the rock matrix has resulted in the net uptake of CO_{2aq}.

The calcite dissolution reaction, which was initiated near the bottom inflow boundary in the rock matrix, resulted in the conversion of CO_{2aq} and the production of Ca^{2+} and HCO_3^-. This simultaneous consumption and production associated with the transport of these species brought the geochemical conditions towards calcite saturation in the transport domain over the period of time. These saturated conditions resulted in calcite precipitation, as demonstrated by the negative calcite reaction rates. However, the calcite reaction rates and the reaction propagation in the matrix were found to be different between the no sorption case and the sorption case. Over the period of time, the calcite kinetic reaction in the rock matrix affected the transport of the CO_{2aq}, Ca^{2+} and HCO_3^- species. After 500 years the spread of CO_{2aq} concentration plume (Figure 4a) was smaller than the concentration plumes of Ca^{2+} and HCO_3^- (Figure 4b and 4c). This difference resulted from the conversion of CO_{2aq} with the simultaneous production of Ca^{2+} and HCO_3^- in the calcite dissolution reaction.

The observed steep variations of normalized mass uptake of CO_{2aq} in geochemical reactions at early times of the simulations in Figures 8, 11 and 12 are due to higher calcite dissolution reaction with associated higher mass uptake of CO_{2aq} relative to the mass inflow through the bottom inlet boundaries. At early times, the lowest saturation state of calcite is caused by leaking CO_2-saturated brine on its entering the transport domain. This results in higher calcite dissolution reaction with associated higher mass uptake of CO_{2aq} relative to the mass inflow. However, over the period of time the saturation state of calcite starts increasing due to production of Ca^{2+} and HCO_3^{-1}, which in turn results in decreasing calcite dissolution reaction with associated lower mass uptake of CO_{2aq}. Also, over time the mass inflow of CO_{2aq} through the bottom inflow boundaries keeps decreasing mainly due to decreasing diffusive fluxes. Thus, after the initial times, almost steady state conditions are reached (mass uptakes of CO_{2aq} Vs its mass inflows) in all the reactive transport scenarios with the exception of

scenario-4 where we observe declining trends of normalized mass uptake at later simulation times.

The retardation in the transport of CO_{2aq} has been observed when one or more physical or geochemical processes are considered (Figure 9, Figure 10a and Figure 10b). Among these physical and geochemical processes, the aqueous phase mass storage of CO_{2aq} in pore spaces of the rock matrix has played an important role in the inhibition of the transport of leaked CO_{2aq}, followed by its sorption in the rock matrix and (to a lesser extent) by the mass uptake of CO_{2aq} in geochemical reactions. The retention of CO_{2aq} due to sorption along the leakage pathway was seen highly dependent on the magnitude of the sorption partitioning coefficient. Thus, properly accounting for sorption is important for evaluating the fate of CO_{2aq} that leaks from the storage reservoir along the leaky pathways.

In Figure 12, the observed variation in the normalized mass uptake of CO_{2aq} in geochemical reactions between the reactive transport scenarios 5, 5a, and 5a was mainly due to different calcite kinetics prevailing in these reactive transport scenarios. Higher temperature in scenarios 5a and 5b resulted in (i) higher calcite kinetic rate constant (9.44×10^{-9} [mol/(s m^2)]) in scenarios 5a and 5b than that in scenario-5 (4.63×10^{-9} [mol/(s m^2)]), and (ii) lower calcite reaction equilibrium constant in scenarios 5a and 5b (16.34) than in scenario-5 (26.76). At very early times, higher kinetic rate constant causes higher calcite dissolution reaction rate in scenarios 5a and 5b compared to that prevailing in scenario-5. At very early times of simulation, higher calcite dissolution reaction rate causes higher mass uptake of CO_{2aq} and thus higher normalized mass uptake in scenarios 5a and 5b compared to that in scenario-5.

As a result of lower equilibrium constant in scenarios 5a and 5b due to higher temperature, the saturation state with respect to calcite was reached at relatively lower values of reaction products (Ca^{2+} and HCO_3^-) and at higher value of reactants (H^+) than those in scenario-5.. Also over the period of time, lower equilibrium constant in scenarios 5a and 5b caused saturation state of calcite to increase more rapidly to a relatively higher value in scenarios 5a and 5b compared to that in scenario-5. The resulting higher saturation state of calcite in scenarios 5a and 5b caused a relatively sharp decrease in calcite dissolution reaction in these scenarios than in scenario-5. As a consequence after only 4.47×10^{-2} years (1.41×10^{6} s), the calcite dissolution reaction rate became higher in scenario-5 than that in scenarios 5a and 5b. This resulted in higher normalized uptake of CO_{2aq} in geochemical reactions in scenario-5 compared to that in scenarios 5a and 5b after 4.47×10^{-2} years. Thus in the very early times of simulation, higher calcite kinetic rate constant causes higher mass uptake whereas after 4.47×10^{-2} years higher saturation state of calcite plays an important role and results in lower mass uptake in scenarios 5a and 5b compared to that in scenario-5.

5. Conclusions

In this study, we presented a reactive transport model to study the leakage of CO_2-saturated brine through a fractured clay caprock. This model considers the relatively fast transport of CO_2-saturated brine in the fracture (by advection, dispersion and diffusion), slow transport in the rock matrix (by diffusion), sorption of CO_{2aq}, and various geochemical reactions including calcite dissolution and precipitation in the rock matrix. The reactive transport problem was solved in terms of chemical components. The presented numerical model showed accurate mass balance of various aqueous species as well as kinetically controlled mineral calcite involved in the reactive transport.

The mobility and spreading of CO_{2aq} along the leakage pathway was found to be controlled by the following factors: the velocity magnitude of the brine in the conducting fracture, the mass exchange between the fracture and the neighboring rock matrix through molecular diffusion, the sorption and the kinetics of calcite mineral in the rock matrix. The kinetics of the calcite reaction resulted in spatial and temporal variations in mass of calcite mineral, the mineral reactive surface area, porosity of the medium, and the effective diffusivity of mobile species in the rock matrix. Calcite dissolution reaction in the rock matrix has caused consumption of CO_{2aq} and reduced its mass along the leakage pathway.

This study has quantified the amount of CO_{2aq} uptake in various aqueous phase equilibrium and calcite kinetic reactions along a fractured pathway under a few hypothetical leakage scenarios. In the reactive transport scenarios considered, the transport retardation in CO_{2aq} and its mass uptake in geochemical reactions along the flow pathway was found to be sensitive to various physical and geochemical processes and parameters. The total mass uptake of CO_{2aq} in geochemical reactions increases with increase in fluid velocity in the fracture, diffusion coefficient and sorption partition coefficient, whereas it decreases with increasing temperature along the leakage pathway. After 500 years of simulation for the selected set of parameters in the various reactive transport scenarios, the normalized mass uptake of CO_{2aq} was found to be 4.43% for the no sorption case and up to 5.46% for the sorption case.

The analysis presented here retains a number of limitations that might be addressed by future studies. In particular, the mineralogical composition of clay caprock considered here is very site specific, and only the kinetics of calcite mineral is considered, thereby ignoring the role of other minerals due to their slow kinetics. Other simplifications include: the idealized geometry of the fracture, the assumption of a constant porosity in the fracture, and the

assumption of constant boundary conditions. Despite these simplifications, this analysis captures the most salient aspects of CO_{2aq} leakage along the fractured pathway in the clay caprock. The reactive transport model presented here can be applied to study the leakage of CO_2-saturated brine in the fractured rock formation where calcite is the major rock forming mineral. Future studies should further extend this modeling framework by considering the velocity field in the fracture and in the rock matrix coupled with the porosity and permeability variations due to mineral dissolution and precipitation.

Acknowledgements. This work was partly funded by the Higher Education Commission (HEC) of Pakistan in the form of scholarship, the Lars Erik Lundberg Scholarship Foundation in Sweden and “STandUp for Energy” the national strategic research project. We give special thanks to the Ministry of Petroleum and Natural Resources of Pakistan for granting the first author the study leave for this research work. XS-V acknowledges support from the ICREA Academia program, and the authors thank two anonymous reviewers for their valuable comments.

APPENDICES

Appendix A: Solution procedure for a system of mixed equilibrium and mineral kinetic reactions

Here we present the methodology of writing the aqueous chemical species in terms of chemical components, formulation of related algebraic equations required for speciation and deriving the reaction term (r_{kin}) that appears in the reactive transport equation.

A.1. Equilibrium reactions for batch geochemical modeling

The five equilibrium reactions considered in the batch reaction modeling are displayed as (R0)-(R4) in Table 1. Despite the presence of brine, the dissolution of NaCl in the reactive system does not need to be calculated because we can assume that halite saturation is not reached and precipitation never occurs. Also considering chloride (Cl^{-1}) as a conservative solute it is fully decoupled from the geochemical system. The activity of H_2O was assumed as unity and is not considered in the list of either primary or secondary species (Saaltink et al., 1998). The equilibrium geochemical system involves seven aqueous chemical species (HCO_3^-, Na^+, CO_{2aq}, H^+, OH^-, CO_3^{2-}, and $NaHCO_{3aq}$). These species, N_s^{eq} (= 7) appear in five N_e (= 5) independent equilibrium reactions.

A.2. Equilibrium reactions for reactive transport modeling

In reactive transport modeling, the equilibrium between the gas (CO_{2g}) and dissolved phase (CO_{2aq}) is not considered and is excluded from the list of equilibrium reactions. Here, the geochemical system involves the same seven aqueous chemical species (N_s^{eq} = 7), which now appear in four equilibrium reactions (N_e = 4). In this study, species Ca^{2+} is only involved in the kinetic reaction of mineral calcite and does not participate in any of the equilibrium reactions. Here, we call this species (Ca^{2+}) the only-kinetic species (N_s^{kin} =1). The species

involved in all of the reactions (equilibrium and kinetic) are classified as primary and secondary. The elimination of the equilibrium reaction term in the reactive transport equation presented by Saaltink et al., 1998 requires that the stoichiometric reaction matrices must be of an appropriate size. Saaltink et al., 1998 presented a method for eliminating equilibrium reactions term in the reactions scenarios, in which the species involved in the kinetic reactions also participate in the equilibrium reactions. In this study, to produce correctly sized matrices (explained below), we also included the only-kinetic species in the list of primary species. Thus, the total number of species involved in the equilibrium plus the kinetic reactions becomes eight ($N_s^{tot} = N_s^{eq} + N_s^{kin}$). The equilibrium reactions are described by the law of mass action and can be written in matrix form as follows:

$$\mathbf{S_{eq}} \log \mathbf{a} = \log \mathbf{K} \qquad \text{(A1)}$$

where $\mathbf{a}$ is the vector of activities of all the aqueous species, $\mathbf{K}$ is the vector of equilibrium reaction constants, and $\mathbf{S_{eq}}$ is a matrix (size $N_e \times N_s^{tot}$) containing the stoichiometric coefficients of the equilibrium reactions. We have selected HCO_3^-, Na^+, CO_{2aq} and Ca^{2+} as the four primary species ($N_s^p = N_s^{tot} - N_e = 4$). The four remaining species (H^+, OH^-, CO_3^{2-} and, $NaHCO_{3aq}$) are designated as secondary. While the only-kinetic species are included in the list of primary species, the stoichiometry of the resulting reaction matrix ensures that the changes in the concentrations of the only-kinetic species only depend on the kinetic reaction and are not affected by any of the equilibrium reactions. With this choice, the equilibrium reaction matrix $\mathbf{S_{eq}}$ is split into two portions that represent the primary and secondary species as follows:

$$\mathbf{S_{eq}} = [\mathbf{S}_1 \quad \mathbf{S}_2] \qquad \text{(A2)}$$

where $\mathbf{S}_1$ is the sub-matrix ($N_e \times N_s^{tot} - N_e$), and $\mathbf{S}_2$ is the square sub-matrix ($N_e \times N_e$). From equilibrium reactions (R1) through (R4) (in Table 1), the actual matrices can be written as follows:

$$\mathbf{S_1} = \begin{bmatrix} HCO_3^- & Na^+ & CO_{2aq} & Ca^{2+} \\ 1 & 0 & -1 & 0 \\ 0 & 0 & 0 & 0 \\ -1 & 0 & 0 & 0 \\ -1 & -1 & 0 & 0 \end{bmatrix}$$

$$\mathbf{S_2} = \begin{bmatrix} H^+ & OH^- & CO_3^{2-} & NaHCO_{3aq} \\ 1 & 0 & 0 & 0 \\ 1 & 1 & 0 & 0 \\ 1 & 0 & 1 & 0 \\ 0 & 0 & 0 & 1 \end{bmatrix}$$

$$\mathbf{S_{eq}} = \begin{bmatrix} HCO_3^- & Na^+ & CO_{2aq} & Ca^{2+} & H^+ & OH^- & CO_3^{2-} & NaHCO_{3aq} \\ 1 & 0 & -1 & 0 & 1 & 0 & 0 & 0 \\ 0 & 0 & 0 & 0 & 1 & 1 & 0 & 0 \\ -1 & 0 & 0 & 0 & 1 & 0 & 1 & 0 \\ -1 & -1 & 0 & 0 & 0 & 0 & 0 & 1 \end{bmatrix}$$

A.3. Reducing the order of the reactive transport system

The reaction term ($\mathbf{r_{kin}}$) in the reactive transport equation can be explicitly written as a linear combination of all the reactions presented in Table 1 ((R1) through (R5)). The coefficients of these linear combinations form a stoichiometric matrix. In short, it is possible to write the following:

$$\mathbf{r_{kin}} = \mathbf{S}^{\mathbf{T}} r \qquad \text{(A3)}$$

This equation can be split into two parts to separately account for the equilibrium and kinetic reactions as follows:

$$\mathbf{r_{kin}} = \mathbf{S_{eq}^T} r_{eq} + \mathbf{S_{kin}^T} r_m \quad \text{(A4)}$$

where $\mathbf{S_{eq}^T}$ is a transpose of $\mathbf{S_{eq}}$, r_m represents the mineral kinetic reaction that is defined in equation (5), and $\mathbf{S_{kin}^T}$ is a transpose of the matrix of all the dissolved species, which represents their stoichiometry in the mineral kinetic reactions ($\mathbf{S_{kin}}$):

$$\mathbf{S_{kin}^T} = \begin{bmatrix} HCO_3^- & Na^+ & CO_{2aq} & Ca^{2+} & H^+ & OH^- & CO_3^{2-} & NaHCO_{3aq} \\ 1 & 0 & 0 & 1 & -1 & 0 & 0 & 0 \end{bmatrix}$$

For the kinetic reactions, the rate can be computed from the activities of the species. However, for the equilibrium reactions, the rates are in principle undetermined. Thus, the equilibrium reaction term is described by equilibrium laws, which are algebraic expressions. The considered geochemical system involves eight chemical species that are involved in equilibrium and mineral kinetic reactions and requires eight transport equations. However, the number of transport equations can be reduced by eliminating the equilibrium reaction term ($\mathbf{r_{eq}}$) (Saaltink et al., 1998). To eliminate the equilibrium reaction rates in the transport equation, a kernel matrix ($\mathbf{U}$) can be defined as follows (Saaltink et al., 1998):

$$\mathbf{U}\mathbf{S_{eq}^T} = 0 \Rightarrow \mathbf{U}\mathbf{S_{eq}^T}\mathbf{r_{eq}} = 0 \quad \text{(A5)}$$

The matrix $\mathbf{U}$ is given as

$$\mathbf{U} = \begin{bmatrix} \mathbf{I}_{N_s^{tot} - N_e} & \left(-\mathbf{S_2^{-1}}\mathbf{S_1}\right)^{\mathbf{T}} \end{bmatrix} \quad \text{(A6)}$$

where $\mathbf{I}_{N_s^{tot}\text{-}N_e}$ denotes the identity matrix with $N_s^{tot} - N_e$ rows and columns. The matrix $\mathbf{U}$ is referred to as the "component matrix" because it adds up the total amount of a chemical component distributed over various aqueous chemical species involved in chemical reactions.

The process of defining the component matrix requires that the matrix $\mathbf{S_2}$ must be invertible. After some algebra, the resulting matrix is written as follows:

$$\mathbf{U} = \begin{pmatrix} \frac{\text{species}}{\text{components}} & HCO_3^- & Na^+ & CO_{2aq} & Ca^{2+} & H^+ & OH^- & CO_3^{2-} & NaHCO_{3aq} \\ u_{HCO_3} & 1 & 0 & 0 & 0 & -1 & 1 & 2 & 1 \\ u_{Na} & 0 & 1 & 0 & 0 & 0 & 0 & 0 & 1 \\ u_{CO_2} & 0 & 0 & 1 & 0 & 1 & -1 & -1 & 0 \\ u_{Ca} & 0 & 0 & 0 & 1 & 0 & 0 & 0 & 0 \end{pmatrix}$$

By pre-multiplying the concentration vector ($\mathbf{c}$) of the species involved in all of the reactions by the component matrix ($\mathbf{U}$), we can obtain the total concentrations of the four chemical components as a linear combination of the dissolved species as follows:

$$\mathbf{u = Uc} \qquad \text{(A7)}$$

where $\mathbf{u}$ is the vector of the total concentrations of the components. Equation (A7) results in the following four chemical components that are involved in the reactive transport equation:

$$\begin{cases} u_{HCO_3} = c_{HCO_3^-} - c_{H^+} + c_{OH^-} + 2c_{CO_3^{2-}} + c_{NaHCO_{3aq}} \\ u_{Na} = c_{Na^+} + c_{NaHCO_{3aq}} \\ u_{CO_2} = c_{CO_{2aq}} + c_{H^+} - c_{OH^-} - c_{CO_3^{2-}} \\ u_{Ca} = c_{Ca^{2+}} \end{cases}$$

for the following components vector ($\mathbf{u}$):

$$\mathbf{u} = \begin{bmatrix} u_{HCO_3} \\ u_{Na} \\ u_{CO_2} \\ u_{Ca} \end{bmatrix}$$

By introducing the component matrix ($\mathbf{U}$), the required number of transport equations has been reduced to four (equal to the number of chemical components) from eight (equal to the number of aqueous species). After eliminating the equilibrium reactions term, the reaction term in equation (A4) is reduced as follows:

$$\mathbf{r_{kin}} = \mathbf{US_{kin}^{T}} r_m \tag{A8}$$

The product of first two terms in equation (A8) results in the following vector:

$$\mathbf{US_{kin}^{T}} = \begin{bmatrix} 2 \\ 0 \\ -1 \\ 1 \end{bmatrix}$$

Thus equation (A8) can be written in the following forms:

$$\mathbf{r_{kin}} = \mathbf{US_{kin}^{T}} r_{kin}^{m} = \begin{bmatrix} 2 \\ 0 \\ -1 \\ 1 \end{bmatrix} \begin{bmatrix} r_m \end{bmatrix} \tag{A9}$$

$$\mathbf{r_{kin}} = \begin{cases} r_{u_{\mathrm{HCO_3}}} = 2r_m \\ r_{u_{\mathrm{Na}}} = 0r_m \\ r_{u_{\mathrm{CO_2}}} = -r_m \\ r_{u_{\mathrm{Ca}}} = r_m \end{cases} \tag{A10}$$

Thus, the reaction term ($\mathbf{r_{kin}}$) in equation (A10) provides information regarding the consumption or production of all four chemical components involved (thereby considering the combined effects of equilibrium and the mineral kinetic reactions) in the reactive transport equation.

A.4. Speciation modeling

We refer to the process of finding the individual aqueous species concentrations from the chemical components as speciation modeling. Because the chemical components have been written as linear combinations of aqueous species, we must solve algebraic equations to calculate the concentration of aqueous species.

A.4.1. Batch geochemical modeling

A system of eight algebraic equations (A11 through A18) results from considered five equilibrium reactions ((R0) through (R4)) and one kinetic reaction (R5) that must be solved for eight dissolved species (HCO_3^-, Na^+, CO_{2aq}, Ca^{2+}, H^+, OH^-, CO_3^{2-} and $NaHCO_{3aq}$). One algebraic equation (A18) emerges from the only-kinetic species (Ca^{2+}). These algebraic equations are solved in COMSOL until the residual of the equations are lower than a certain tolerance limit.

$$\left(c_{\mathrm{CO_{2aq}}}\gamma_{\mathrm{CO_{2aq}}}\right)-\left(\mathrm{K}_{\mathrm{CO_{2g}}}\right)=0 \tag{A11}$$

$$\left(c_{\mathrm{H^+}}\gamma_{\mathrm{H^+}}c_{\mathrm{HCO_3^-}}\gamma_{\mathrm{HCO_3^-}}\right)-\left(c_{\mathrm{CO_{2aq}}}\gamma_{\mathrm{CO_{2aq}}}\mathrm{K}_{\mathrm{CO_{2aq}}}\right)=0 \tag{A12}$$

$$\left(c_{\mathrm{H^+}}\gamma_{\mathrm{H^+}}c_{\mathrm{OH^-}}\gamma_{\mathrm{OH^-}}\right)-\left(\mathrm{K}_{\mathrm{H_2O}}\right)=0 \tag{A13}$$

$$\left(c_{\mathrm{H^+}}\gamma_{\mathrm{H^+}}c_{\mathrm{CO_3^{2-}}}\gamma_{\mathrm{CO_3^{2-}}}\right)-\left(c_{\mathrm{HCO_3^-}}\gamma_{\mathrm{HCO_3^-}}\mathrm{K}_{\mathrm{HCO_3^-}}\right)=0 \tag{A14}$$

$$\left(c_{\mathrm{NaHCO_{3aq}}}\gamma_{\mathrm{NaHCO_{3aq}}}\right)-\left(c_{\mathrm{Na^+}}\gamma_{\mathrm{Na^+}}c_{\mathrm{HCO_3^-}}\gamma_{\mathrm{HCO_3^-}}\mathrm{K}_{\mathrm{Na^+}}\right)=0 \tag{A15}$$

$$u_{\mathrm{HCO_3}}-\left(c_{\mathrm{HCO_3^-}}-c_{\mathrm{H^+}}+c_{\mathrm{OH^-}}+2c_{\mathrm{CO_3^{2-}}}+c_{\mathrm{NaHCO_{3aq}}}\right)=0 \tag{A16}$$

$$u_{\mathrm{Na}}-\left(c_{\mathrm{Na^+}}+c_{\mathrm{NaHCO_{3aq}}}\right)=0 \tag{A17}$$

$$u_{\mathrm{Ca}}=c_{\mathrm{Ca^{2+}}} \tag{A18}$$

In the equations above, the symbol γ_i represents the activity coefficient of the aqueous species. The detailed methodology of calculating the activity coefficient of aqueous species is presented in Appendix B.

A.4.1.1. Solution of component species

In the batch geochemical modeling, the component species are defined in terms of ordinary differential equations (ODEs) as follows:

$$u_{\mathrm{HCO_3}} = \frac{d}{dt} u_{\mathrm{HCO_3}} - r_{u_{\mathrm{HCO_3}}} \tag{A19}$$

$$u_{\mathrm{Na}} = \frac{d}{dt} u_{\mathrm{Na}} - r_{u_{\mathrm{Na}}} \tag{A20}$$

$$u_{\mathrm{Ca}} = \frac{d}{dt} u_{\mathrm{Ca}} - r_{u_{\mathrm{Ca}}} \tag{A21}$$

In the above equations, the symbol r represents the reaction rates of the respective chemical components which have been defined in equation (A10).

A.4.2. Reactive transport

Transport of the chemical components by the reactive transport equation requires the calculation of the aqueous species at every node of the computational domain for their participation in the equilibrium and kinetic reactions. The following eight algebraic equations (A22 through A29) resulted from four equilibrium reactions ((R1) through (R4)) and one mineral kinetic reaction (R5):

$$\left(c_{\mathrm{H^+}} \gamma_{\mathrm{H^+}} c_{\mathrm{HCO_3^-}} \gamma_{\mathrm{HCO_3^-}} \right) - \left(c_{\mathrm{CO_{2aq}}} \gamma_{\mathrm{CO_{2aq}}} \mathrm{K}_{\mathrm{CO_{2aq}}} \right) = 0 \tag{A22}$$

$$\left(c_{\mathrm{H^+}} \gamma_{\mathrm{H^+}} c_{\mathrm{OH^-}} \gamma_{\mathrm{OH^-}} \right) - \left(\mathrm{K}_{\mathrm{H_2O}} \right) = 0 \tag{A23}$$

$$\left(c_{\mathrm{H^+}} \gamma_{\mathrm{H^+}} c_{\mathrm{CO_3^{2-}}} \gamma_{\mathrm{CO_3^{2-}}} \right) - \left(c_{\mathrm{HCO_3^-}} \gamma_{\mathrm{HCO_3^-}} \mathrm{K}_{\mathrm{HCO_3^-}} \right) = 0 \tag{A24}$$

$$\left(c_{\mathrm{NaHCO_{3aq}}} \gamma_{\mathrm{NaHCO_{3aq}}} \right) - \left(c_{\mathrm{Na^+}} \gamma_{\mathrm{Na^+}} c_{\mathrm{HCO_3^-}} \gamma_{\mathrm{HCO_3^-}} \mathrm{K}_{\mathrm{Na^+}} \right) = 0 \tag{A25}$$

$$u_{\mathrm{HCO_3}} - \left(c_{\mathrm{HCO_3^-}} - c_{\mathrm{H^+}} + c_{\mathrm{OH^-}} + 2c_{\mathrm{CO_3^{2-}}} + c_{\mathrm{NaHCO_{3aq}}} \right) = 0 \tag{A26}$$

$$u_{\mathrm{Na}} - \left(c_{\mathrm{Na}^+} + c_{\mathrm{NaHCO_{3aq}}} \right) = 0 \quad \text{(A27)}$$

$$u_{\mathrm{CO_2}} - \left(c_{\mathrm{CO_{2aq}}} + c_{\mathrm{H}^+} - c_{\mathrm{OH}^-} - c_{\mathrm{CO_3^{2-}}} \right) = 0 \quad \text{(A28)}$$

$$u_{\mathrm{Ca}} = c_{\mathrm{Ca}^{2+}} \quad \text{(A29)}$$

Because one aqueous species (Ca^{2+}) only participates in the kinetic reaction of mineral calcite, its concentration is equal to the respective chemical component that is being transported by the reactive transport equation.

Appendix B: Activity coefficients of aqueous species

The activities of aqueous species are related to their concentration (c) through the activity coefficient (γ) as follows (Lide et al., 2010):

$$a_i = \gamma_i \frac{c_i}{c_0} \quad \text{(B1)}$$

where c_0 is the standard concentration [1 mol/(kg water)], c_i is the molality [mol/(kg water)] of the i-th species of the solution and γ_i is the concentration dependent activity coefficient. The species activity is thus a dimensionless quantity.

The activity coefficients depend on the ionic strength (μ) of the solution defined as follows:

$$\mu = \frac{1}{2} \sum c_i z_i^2 \quad \text{(B2)}$$

A summation is extended over all charged species (c_i), and z_i represents the charge of species i.

B.1. CO_{2aq}

A virial expansion based on excess Gibbs free energy from (Pitzer, 1973) is used to calculate the activity coefficient of CO_{2aq} as follows (Duan & Sun, 2003):

1118 $$\ln\gamma_{CO_2} = 2\lambda_{CO_2\text{-}Na}\left(c_{Na^+} + c_{K^+} + 2c_{Ca^{2+}} + 2c_{Mg^{2+}}\right) - \xi_{CO_2\text{-}Na\text{-}Cl}\left(c_{Cl^-}\right)\left(c_{Na^+} + c_{K^+} + c_{Ca^{2+}} + c_{Mg^{2+}}\right) - 0.07c_{SO_4^{2-}} \quad \text{(B3)}$$

1119 *B.2. Charged species*

1120 The activity coefficients of charged aqueous species for low-ionic strength solutions (up to 3
1121 molal of NaCl dominant solutions) are obtained from the extended Debye-Hückel function
1122 (B-dot model) as follows:

1123 $$\log\gamma_i = -A_\gamma\left(z^2\right)\sqrt{\bar{I}}\Big/\left(1+\dot{a}B_\gamma\sqrt{\bar{I}}\right)+\dot{B}\bar{I} \quad \text{(B4)}$$

1124 *B.3. Uncharged species*

1125 The activity coefficients of the electrically neutral, non-polar species are calculated from the
1126 following relationship (Betheke, 2008):

1127 $$\log\gamma_j = aI + bI^2 + cI^3 \quad \text{(B5)}$$

1128 with the corresponding parameters available in Table B 1. Linear interpolation is used to find
1129 the values of the constants (a, b and c) at the temperature of interest.

1130 **Table B 1.** Parameters for equation (B5).

T [°C]	a	b	c
25	0.1127	-0.01049	1.545×10^{-3}
100	0.08018	-0.001503	0.5009×10^{-3}
200	0.09892	-0.01040	1.386×10^{-3}
300	0.1967	-0.01809	-2.497×10^{-3}

1131

1132 *B.4. Water*

1133 Although different models are available for evaluating the activity of water, the activity of
1134 water is assumed as constant and equal to unity in this study (Saaltink et al., 1998).

Appendix C: Viscosity of brine

According to Mao & Duan, 2009, the viscosity of brine ($NaCl+H_2O$) can be determined from the following relationship:

$$\mu_{sol} = \mu_r \mu_{H_2O} \quad \text{(C1)}$$

where μ_{sol} represents the solution viscosity [Pa s], μ_r refers to the relative viscosity, and μ_{H_2O} is the viscosity of pure water in [Pa s]. The relative viscosity is found from the following relationship:

$$\mu_r = \exp\left(Am + Bm^2 + Cm^3\right) \quad \text{(C2)}$$

where m is the molality [mol/(kg water)] of salt (NaCl) and A, B, and C are polynomials defined as a function of temperature T [K]:

$$\begin{cases} A = a_0 + a_1 T + a_2 T^2 \\ B = b_0 + b_1 T + b_2 T^2 \\ C = c_0 + c_1 T \end{cases} \quad \text{(C3)}$$

The parameters (a_i, b_i and c_i) are given in Table C 1.

Table C 1. Parameters for equation (C3).

i	a_i	b_i	c_i
0	-0.21319213	0.69161945×10^{-1}	-0.2598886×10^{-2}
1	0.1365159×10^{-2}	-0.2729226×10^{-3}	0.7798923×10^{-5}
2	-0.1219176×10^{-5}	0.2085245×10^{-6}	—

The viscosity of pure water was calculated from the following relationship:

$$\mu_{H_2O} = \exp\left(\sum_{i=1}^{5} d_i T^{i-3} + \sum_{i=6}^{10} d_i \rho_{H_2O} T^{i-8}\right) \quad \text{(C4)}$$

where the density of pure water (ρ_{H_2O}) was found from Cooper & Dooley, 2007 and the parameters (d_i) are given in Table C 2.

Table C 2. Parameters for equation (C4).

i	d_i	i	d_i
1	0.28853170×10^{7}	6	-0.19283851×10^{7}
2	-0.11072577×10^{5}	7	0.56216064×10^{4}
3	-0.90834095×10^{1}	8	0.13827250×10^{2}
4	0.30925651×10^{-1}	9	-0.47609523×10^{-1}
5	-0.27407100×10^{-4}	10	0.35545041×10^{-4}

References

Al-Rawajfeh, A.E., 2004. Modeling and simulation of CO_2 release in multiple-effect distillers for seawater desalination, Ph.D. Dissertation. Department of Engineering Sciences, Institute of Thermal Process Engineering, Martin-Luther University of Halle-Wittenberg, Halle(Saale), Germany.

Andreani, M., Gouze, P., Luquot, L., Jouanna, P., 2008. Changes in seal capacity of fractured claystone caprocks induced by dissolved and gaseous CO_2 seepage. Geophys. Res. Lett. 35, L14404. doi:10.1029/2008GL034467.

Arts, R., Chadwick A., Eiken, O., 2005. Recent time-lapse seismic data show no indication of leakage at the Sleipner CO_2-injection site. Greenhouse Gas Control Technologies, Volume 1.

Audigane, P., Gaus, I., Pruess, K., Xu, T., 2005. Reactive transport modeling using TOUGHREACTE for the long term CO_2 storage at Sleipner, Nort Sea. Conference Proceedings, 4th Annual conference on carbon capture and sequestration DOE/NETL, May 2-5, 2005.

Audigane, P., Gaus, I., Czernichowski-Lauriol, I., Pruess, K., Xu, T., 2007. Two-dimensional reactive transport modeling of CO_2 injection in a saline aquifer at the Sleipner site, North Sea. Am. J. Sci. 307 (7), 974-1008. doi:10.2475/07.2007.02.

Bachu, S., Gunter, W.D., and Perkins, E.H., 1994. Aquifer disposal of CO_2: hydrodynamic and mineral trapping. Energ. Convers. Manage. 35(4), 269-279.

Bear, J., Cheng, A.H..-D., 2010. Modeling groundwater flow and contaminant transport. Vol. 23, ISBN, 978-1-4020-6681-8, Springer, Dordrecht. doi:10.1007/978-1-4020-6682-5.

Betheke, C.M., 2008. Geochemical and Biogeochemical Reaction Modeling, second ed., ISBN-13 978-0-511-37897-3. Cambridge University Press, New York.

1181 Bodin, J., Delay, F., de Marsily, G., 2003. Solute transport in a single fracture with negligible
1182 matrix permeability: 2. Mathematical formalism. Hydrogeol. J 11 (4), 434-454.
1183 doi:10.1007/s10040-003-0269-1.
1184 COMSOL. The Platform for Physics-Based Modeling and Simulation. COMSOL AB,
1185 Stockholm, Sweden.
1186 Cooper, J.R., and Dooley, R.B., 2007. IAPWS-IF97, Revised release on the IAPWS Industrial
1187 Formulation 1997 for the Thermodynamic Properties of Water and Steam (The revision
1188 only relates to the extension of region 5 to 50 MPa). The International Association for
1189 the Properties of Water and Steam.
1190 Cvetkovic, V., Selroos, J.O., Cheng, H., 1999. Transport of reactive tracers in rock
1191 fractures. J. Fluid Mech. 378, 335-356. doi:10.1017/S0022112098003450.
1192 Dreybrodt, W., Lauckner, J., Zaihua, L., Svensson, U., and Buhmann, D., 1996. The kinetics
1193 of the reaction in the $CO_2+H_2O\rightarrow H^++HCO_3^-$ as one of the rate limiting steps for the
1194 dissolution of calcite in the system H_2O-CO_2-$CaCO_3$, Geochemica et Cosmochimica
1195 Acta, 60(18), 3375-3381.
1196 Dreybrodt, W., Eisenlohr, L., Madry, B., and Ringer, S., 1997. Precipitation kinetics of calcite
1197 in the system $CaCO_3$-H_2O-CO_2: The conversion to CO_2 by the slow process $H^++HCO_3^-$
1198 $\rightarrow CO_2+H_2O$ as a rate limiting step, Geochemica et Cosmochimica Acta, 61(18), 3897-
1199 3904.
1200 Duan, Z., Sun, R., 2003. An improved model calculating CO_2 solubility in pure water and
1201 aqueous NaCl solutions from 273 to 533 K and from 0 to 2000 bar. Chem. Geol. 193 (3-
1202 4), 257-271. doi:10.1016/S0009-2541(02)00263-2.
1203 Duan, Z., Sun, R., Zhu, C., Chou, I., 2006. An improved model for the calculation of CO_2
1204 solubility in aqueous solutions containing Na^+, K^+, Ca^{2+}, Mg^{2+}, Cl^-, and SO_4^{2-}. Mar.
1205 Chem. 98 (2-4), 131-139. doi:10.1016/j.marchem.2005.09.001.

1206 Ellis, B.R., Bromhal, G.S., McIntyre, D.L., Peters, C.A., 2011. Changes in caprock integrity
1207 due to vertical migration of CO_2-enriched brine. Energ. Procedia 4, 5327-5334.
1208 Fujii, T., Nakagawa, S., Sato, Y., Inomata, H., Hashida, T., 2010. Sorption characteristics of
1209 CO_2 on rocks and minerals in storing CO_2 processes. Natural Res. 1 (1), 1-10.
1210 Gaus, I., 2010. Role and impact of CO_2-rock interactions during CO_2 storage in sedimentary
1211 rocks. Int. J. Greenh. Gas Con. 4 (1), 73-89. doi:10.1016/j.ijggc.2009.09.015.
1212 Gherardi, F., Xu, T., Pruess, K., 2007. Numerical modeling of self-limiting and self-
1213 enhancing caprock alteration induced by CO_2 storage in a depleted gas reservoir. Chem.
1214 Geol. 244 (1-2), 103-129. doi:10.1016/j.chemgeo.2007.06.009.
1215 Grisak, G.E., Pickens, J.F., 1980. Solute transport through fractured media 1. The effect of
1216 matrix diffusion. Water Resour. Res. 16 (4), 719-730.
1217 Gunter, W.D., Perkins, E.H., and McCANN, T.J., 1993. Aquifer disposal of CO_2-rich gases:
1218 reaction design for added capacity. Energy Convers. Mgmt Vol. 34(9-11), 941-948.
1219 Hassanzadeh, H., Pooladi-
1220 Darvish, M., Elsharkawy, A.M., Keith, D.W., Leonenko, Y., 2008. Predicting PVT data
1221 for CO_2-brine mixtures for black-oil simulation of CO_2 geological storage. Int. J.
1222 Greenh. Gas Con. 2, 65-77.
1223 Haugan, P.M., Joos, F., 2004. Metrics to assess the mitigation of global warming by carbon
1224 capture and storage in the ocean and in geological reservoirs. Geophys. Res. Lett.
1225 31, L18202.
1226 Heller, R., and Zoback, M., 2014. Adsorption of methane and carbon dioxide on gas shale and
1227 pure mineral samples. Unconventional Oil Gas Resour. 8, 14-24.
1228 Hellevang, H., 2006. Interactions between CO_2, Saline Water and Minerals during Geological
1229 Storage of CO_2, Ph.D. Thesis. University of Bergen, Norway.

1230 Holloway, S., 1997. An overview of the underground disposal of carbon dioxide. Energ.
1231 Convers. Manage. 38, S193-S198. doi:10.1016/S0196-8904(96)00268-3.
1232 Holloway, S., 2005. Underground sequestration of carbon dioxide-a viable greenhouse gas
1233 mitigation option. Energy 30 (11-12), 2318-2333. doi:10.1016/j.energy.2003.10.023.
1234 Intergovernmental Panel of Climate Change, 2002. IPCC Workshop on Carbon Dioxide
1235 Capture and Storage, Proceedings. Regina, Canada.
1236 Intergovernmental Panel of Climate Change, 2005. IPCC Special Report on Carbon Dioxide
1237 Capture and Storage. Cambridge University Press, New York, America.
1238 Johnson, J.W., Nitao, J.J., and Knauss K.G., 2004. Reactive transport modelling of CO_2
1239 storage in saline aquifers to elucidate fundamental processes, trapping mechanisms,
1240 and sequestration partitioning. Geological Society of London Special Publication on
1241 Carbon Sequestration Technologies.
1242 Kaufmann, G., Dreybrodt, W., 2007. Calcite dissolution kinetics in the system $CaCO_3$-H_2O-
1243 CO_2 at high undersaturation. Geochim. Cosmochim. Acta 71 (6), 1398-1410.
1244 doi:10.1016/j.gca.2006.10.024.
1245 Lai, K-H., Chen, J-S., Liu, C-W., and Yang, S-Y., 2014. Effect of permeability-porosity
1246 functions on simulated morphological evolution of a chemical dissolution front. Hydrol.
1247 Process. 28, 16-24. doi: 10.1002/hyp.9492.
1248 Langmuir D, 1997. Aqueous Environmental Geochemistry. ISBN 0-02-367412-1, Prentice
1249 Hall, New Jersey.
1250 Lasaga, A.C., 1984. Chemical kinetics of water-rock interaction. J. Geophys. Res. 89
1251 (B6), 4009-4025.
1252 Lasaga, A.C., Soler, J.M., Ganor, J., Bruch, T.E., Nagy, K.L., 1994. Chemical weathering rate
1253 laws and global geochemical cycles. Geochim. Cosmochim. Acta 58 (10), 2361-2386.

Lide D.R., ed., 2010. CRC Handbook of Chemistry and Physics. 90th Edition (CD-ROM Version 2010), CRC Press/Taylor and Francis, Boca Raton, FL.Mao, S., Duan, Z., 2009. The viscosity of aqueous alkali-chloride solutions up to 623K, 1000 bar, and high ionic strength. Int. J. Thermophys. 30 (5), 1510-1523. doi:10.1007/s10765-009-0646-7.

Mao S., and Duan Z. (2009), The viscosity of aqueous alkali-chloride solutions up to 623K, 1000 bar, and high ionic strength, Int. J. Thermophys., 30, 1510-1523.

Marini, L., 2007. Sequestration of carbon dioxide; thermodynamics kinetics and reaction path modeling. ISBN-13:978-0-444-52950-3. Elsevier, Netherlands and UK.

Middleton, R.S., Keating, G.N., Stauffer, P.H., Jordan, A.B., Viswanathan, H.S., Kang, Q.J., 2012. The cross-scale science of CO2 capture and storage: from pore scale to regional scale. Energ. Environ. Sci. 5 (6), 7328-7345. doi:10.1039/c2ee03227a.

Neretnieks, I., 1980. Diffusion in the rock matrix: an important factor in radionuclide retardation? J. Geophys. Res. 85 (B8), 4379-4397. doi:10.1029/JB085iB08p04379.

Nogues, J.P., Fitts, J.P., Celia, M.A., Peters, C.A., 2013. Permeability evolution due to dissolution and precipitation of carbonates using reactive transport modeling in pore networks. Water Resour. Res. 49, 6006-6021. doi:10.1002/wrcr.20486.

Novak, C.F., 1993. Modeling mineral dissolution and precipitation in dual-porosity fracture-matrix system. J. Cont. Hydrol. 13, 91-115.

Novak, C.F., 1996. Development of the FMT chemical transport simulator: coupling aqueous density and mineral volume fraction to phase compositions. J. Cont. Hydrol. 21 (1-4), 297-310. doi:10.1016/0169-7722(95)00055-0.

Orr, Jr., F.M., 2009. CO_2 capture and storage: are we ready? Energ. Environ. Sci. 2 (5), 449-458. doi:10.1039/b822107n.

1278 Peters, C.A., Fitts, J.P., Wilson, E.J., Pollak, M.F., Bielicki, J.M., and Bhatt, V., 2014. Basin-
1279 scale leakage risks from geologic carbon sequestration: impact on carbon capture and
1280 storage energy market competitiveness. Final Scientific/Technical Report,
1281 DOE/FE0000749-41, Princeton University, Princeton, NJ, United States.
1282 Pitzer, S.K., 1973. Thermodynamics of electrolytes. I. Theoretical basis and General
1283 equations. J. Phys. Chem. 77 (2), 268-277.
1284 Pokrovsky, O.S., Golubev, S.V., Schott, J., Castillo, A., 2009. Calcite, dolomite and
1285 magnesite dissolution kinetics in aqueous solutions at acid to circumneutral pH, 25 to
1286 150 °C and 1 to 55 atm pCO_2: new constraints on CO_2 sequestration in sedimentary
1287 basins. Chem. Geol. 265, 20-32.
1288 Pruess, K., 2005. Numerical studies of fluid leakage from a geologic disposal reservoir for
1289 CO_2 show self-limiting feedback between fluid flow and heat transfer. Geophys. Res.
1290 Letters. Vol. 32, L14404, doi: 10.1029/2005GL023250.
1291 Pruess, K., 2006(a). Numerical modeling of CO_2 sequestration in geologic formations-recent
1292 results and open challenges. Earth Sciences Division, Lawrence Berkeley National
1293 Laboratory, University of Californai, Berkeley, CA 94720, USA.
1294 Pruess, K., 2006(b). On leakage from geologic storage reservoirs of CO_2. LBNL-59732.
1295 Lawrence Berkeley National Laboratory.
1296 Pruess, K., 2008. Leakage of CO_2 from geologic storage: Role of secondary accumulation at
1297 shallow depth. Int. J. Greenh. Gas Con. 2, 37-46.
1298 Saaltink, M.W., Ayora, C., Carrera, J., 1998. A mathematical formulation for reactive
1299 transport that eliminates mineral concentrations. Water Resour. Res. 34(7), 1649-1656.
1300 Santschi, C.h, Rossi, M.J., 2006. Uptake of CO_2, SO_2, HNO_3 and HCl on calcite ($CaCO_3$) at
1301 300 K: mechanism and the role of adsorbed water. J. Phys. Chem. A 110 (21), 6789-
1302 6802. doi:10.1021/jp056312b.

1303 Steefel, C.I., Lasaga, A.C., 1994. A coupled model for transport of multiple chemical species
1304 and kinetic precipitation/dissolution reactions with application to reactive flow in single
1305 phase hydrothermal systems. Am.. J. Sci. 294 (5), 529-592. doi:10.2475/ajs.294.5.529.
1306 Steefel, C.I., Lichtner, P.C., 1998(a). Multicomponent reactive transport in discrete fractures
1307 I. Controls on reaction front geometry. J. Hydro. 209, 186-199.
1308 Steefel, C.I., Lichtner, P.C., 1998(b). Multicomponent reactive transport in discrete fractures
1309 II. Infiltration of hyperalkaline groundwater at Maqarin, Jordan, a natural analogue
1310 site. J. Hydro. 209, 200-224.
1311 Stone, E.J., Lowe, J.A., Shine, K.P., 2009. The impact of carbon capture and storage on
1312 climate. Energ. Environ. Sci. 2 (1), 81-91. doi:10.1039/b807747a.
1313 Svensson, U., Dreybrodt, W., 1992. Dissolution kinetics of natural calcite minerals in CO_2-
1314 water systems approaching calcite equilibrium. Chem. Geol. 100, 129-145.
1315 Tabrizy, V.A., Hamouda, A.A., Soubeyrand-Lenoir, E., Denoyel, R., 2013. CO_2 adsorption
1316 isotherm on modified calcite, quartz, and kaolinite surfaces: surface energy analysis.
1317 Pet. Sci. Tech. 31 (15), 1532-1543.
1318 The GEOCHEMIST'S WORKBENCH. An integrated geochemical modeling package.
1319 Aqueous Solutions LLC, Champaign, IL 61820 USA.
1320 Xu, S., Wörman, A., Dverstorp, B., 2001. Heterogeneous matrix diffusion in crystalline rock--
1321 implications for geosphere retardation of migrating radionuclides. J. Contam. Hydrol.
1322 47 (2-4), 365-378.
1323 Xu, T., Sonnenthal, E., Spycher, N., and Zheng, L., 2014. TOUGHREACT V3.0-OMP
1324 Reference Manual: A parallel simulation program for non-isothermal multiphase
1325 geochemical reactive transport. LBNL-DRAFT, Earth Sciences Division, Lawrance
1326 Berkeley National Laboratory, University of California, Berkeley, CA 94720.

Yeh, G-T., and Tripathi, V.S., 1991. A model for simulating transport of reactive multispecies components: model development and demonstration. Water Resour. Res. 27(12), 3075-3094.

Figure captions

Figure 1. Schematic of the transport domain (clayey caprock containing a vertical fracture) lying above the CO_2 geological storage reservoir.
Figure 2. Saturation state of calcite at onset (1 s) of the simulation for (a); scenario-4 (without sorption); and (b) scenario-5 (with sorption).
Figure 3. Calcite reaction rate [mol/(s kg water)] at onset (1 s) of the simulation for; (a) scenario-4 (without sorption); and (b) scenario-5 (with sorption).
Figure 4. Spatial distribution of the concentrations [mol/(kg water)] of dissolved species after 500 years for scenario-5; (a) CO_{2aq}; (b) Ca^{2+}; and (c) HCO_3^{-1}.
Figure 5. Effects of the calcite reaction on the; (a) mass of calcite [mol/(m^3 bulk volume)] for scenario-5; (b) calcite reactive surface area [m^2/(kg water)] for scenario-5 after 500 years.
Figure 6. Effects of the calcite reaction on (a) medium porosity for scenario-5; (b) medium permeability [m^2] for scenario-5; (c) effective diffusivity [m^2/s] for scenario-5 after 500 years.
Figure 7. Evolution of pH in the fracture-matrix system after 500 years for various base-case transport scenarios; (a) scenario-2 (no calcite reaction, no sorption); (b) scenario-3 (no calcite reaction with sorption); (c) scenario-4 (calcite reaction, no sorption); and (d) scenario-5 (calcite reaction with sorption).
Figure 8. The percent normalized uptake of CO_{2aq} in aqueous phase and calcite kinetic reactions without sorption (scenario-4) and with sorption (scenario-5).
Figure 9. Breakthrough curve for the base-case transport scenario-1 showing the concentration of CO_{2aq} at top outflow of the fracture over the period of time.
Figure 10. Breakthrough curves showing the concentration of CO_{2aq} for various base-case transport scenarios along the fracture, at; (a) 10 m from the inflow boundary; and (b) 20 m from the inflow boundary.
Figure 11. The percent normalized uptake of CO_{2aq} in aqueous phase and calcite kinetic reactions for various reactive transport scenarios (5.1, 5.2, 5.3, and 5.4) studied in the sensitivity analysis.
Figure 12. The percent normalized mass uptake of CO_{2aq} in aqueous phase and calcite kinetic reactions for pressure and temperature conditions of: (i) 105 bar and 45°C (scenario-5); and (ii) 155 bar and 60°C (scenario-5a).

Tables

Table 1. Chemical reactions considered for $CaCO_3$-H_2O-CO_2 system.

No.	Reactions and equilibrium reaction constants
(R0)[1]	$CO_{2g} \leftrightarrow CO_{2aq}$
(R1)[2]	$H_2O + CO_{2aq} \leftrightarrow H^+ + HCO_3^-$
(R2)[2]	$H_2O \leftrightarrow H^+ + OH^-$
(R3)[2]	$HCO_3^- \leftrightarrow H^+ + CO_3^{2-}$
(R4)[2]	$Na^+ + HCO_3^- \leftrightarrow NaHCO_{3aq}$
(R5)[2]	$CaCO_3 + H^+ \leftrightarrow Ca^{2+} + HCO_3^-$

1. Equilibrium reaction constant is based on Duan & Sun, 2003 as modified by Duan et al., 2006; 2. Equilibrium reaction constants are taken from The Geochemist's Workbench (GWB) (default thermodynamic data for the GWB).

Table 2. Clay caprock mineralogical composition (Gherardi et al., 2007).

Minerals	Volume fraction in solid rock	Volume fraction in porous rock (12% porosity)
Calcite	0.29	0.255
Dolomite	0.04	0.035
Quartz	0.20	0.176
Illite	0.02	0.018
K-feldspar	0	0
Chlorite	0.06	0.053
Albite	0	0
Kaolinite	0.05	0.044
Na-smectite	0.15	0.132
Muscovite	0.19	0.1672

Table 3. Parameters and initial values of variables used in equations (4)-(6) for mineral calcite.

k_{25}* [mol/(s m^2)]	E_a* [KJ/mol]	A_m** [m^2/(kg water)]	$c_{m,bulk}$** [mol/(m^3 bulk volume)]
1.60×10-9	41.87	38.68	6912.5

* From Svensson & Dreybrodt, 1992; **Initial values are calculated from initial volume fraction (corresponding to initial caprock porosity of 0.12) of minerals in porous rock matrix. The minerals reactive surface area is taken equal to 10% of the calculated physical surface area of the respective minerals.

Table 4. Calculated values of viscosities and molecular diffusion coefficients at various pressure and temperature conditions.

Pressure and Temperature	μ_0 [Pa s]	μ_b[Pa s]	D_0 [m^2/s]	D_b[m^2/s]
105 bar and 45℃	5.96×10^{-4}	6.27×10^{-4}	3.19×10^{-9}	3.05×10^{-9}
155 bar and 60℃	4.69×10^{-4}	4.94×10^{-4}	4.25×10^{-9}	4.05×10^{-9}

Table 5. Values of sorption partition coefficient K_d [m^3/kg] deduced from Heller & Zoback, 2014.

Clay sample	Barnett 31	Marcellus	Montney	Eagle Ford 127
Calcite content (%)	0	1	8.1	80
Clay content (%)	37.4	52	24.1	5
K_d [m^3/kg] value at 10.5 MPa	3.18×10^{-3}	1.54×10^{-3}	3.33×10^{-3}	7.39×10^{-4}
K_d [m^3/kg] value at 15.5 MPa	3.45×10^{-3}	1.62×10^{-3}	3.60×10^{-3}	7.93×10^{-4}

Table 6. Initial (sub-index 0) and boundary conditions (sub-index bc).

Pressure and temperature	45°C and 105 bar	60°C and 155 bar
Component species	Concentration [mol/(kg water)]	Concentration [mol/(kg water)]
$u_{HCO_{3,0}}$	4.02×10^{-3}	3.10×10^{-3}
u_{Na_0}	5.00×10^{-1}	5.00×10^{-1}
u_{Ca_0}	2.01×10^{-3}	1.55×10^{-3}
$u_{CO_{2,0}}$	1.82×10^{-4}	1.38×10^{-4}
$u_{HCO_{3,bc}}$	7.17×10^{-2}	5.95×10^{-2}
$u_{Na_{bc}}$	5.00×10^{-1}	5.00×10^{-1}
$u_{Ca_{bc}}$	3.58×10^{-2}	2.97×10^{-2}
$u_{CO_{2,bc}}$	1.08	1.06

Table 7. Various base-case transport scenarios.

Scenarios	Processes accounted for
1	No interaction between fracture and matrix
2	Molecular diffusion between fracture and matrix, no calcite mineral reaction in the matrix, no sorption in the matrix
3	Molecular diffusion between fracture and matrix, no calcite mineral reaction in the matrix, sorption in the matrix
4	Molecular diffusion between fracture and matrix, calcite mineral reaction in the matrix, no sorption in the matrix
5	Molecular diffusion between fracture and matrix, calcite mineral reaction in the matrix, sorption in the matrix

Table 8. Sensitivity analysis for various parameters using the base-case transport scenarios 3 and 5.

Sub-scenarios	Velocity in the fracture, v [m/s]	Distribution coefficient, K_d [m^3/kg]	Pressure and temperature

3.1	$3.17x10^{-8}$	$2.50x10^{-4}$	105 bar and 45°C
3.2	$6.34x10^{-7}$	$2.50x10^{-4}$	105 bar and 45°C
3.3	$3.17x10^{-7}$	$7.50x10^{-4}$	105 bar and 45°C
3.4	$3.17x10^{-7}$	$8.33x10^{-5}$	105 bar and 45°C
5.1	$3.17x10^{-8}$	$2.50x10^{-4}$	105 bar and 45°C
5.2	$6.34x10^{-7}$	$2.50x10^{-4}$	105 bar and 45°C
5.3	$3.17x10^{-7}$	$7.50x10^{-4}$	105 bar and 45°C
5.4	$3.17x10^{-7}$	$8.33x10^{-5}$	105 bar and 45°C
3a	$3.17x10^{-7}$	$2.50x10^{-4}$	155 bar and 60°C
5a	$3.17x10^{-7}$	$2.50x10^{-4}$	155 bar and 60°C

Table 9. Species concentrations from the background BGM at 45°C and 0.01 bar (column 2) and from CO_{2g} dissolution reaction modeling performed at 45°C and 105 bar (column 3).

Pressure and temperature	45°C and 0.01 bar	45°C and 105 bar
Species	c [mol/(kg water)]	c [mol/(kg water)]
HCO_3^-	3.33×10^{-3}	6.04×10^{-2}
Na^+	4.99×10^{-1}	4.89×10^{-1}
Cl^-	5.00×10^{-1}	5.00×10^{-1}
Ca^{2+}	2.01×10^{-3}	3.58×10^{-2}
CO_{2aq}	1.98×10^{-4}	1.08
H^+	5.44×10^{-8}	1.67×10^{-5}
OH^-	1.29×10^{-6}	4.25×10^{-9}
CO_3^{2-}	1.43×10^{-5}	8.85×10^{-7}
$NaHCO_{3aq}$	6.63×10^{-4}	1.13×10^{-2}

Table 10. Mass balance [mol] of CO_{2aq} in the base-case reactive transport scenarios 4 and 5.

Scenarios	Scenario-4	Scenario-5
Total mass entered the domain	1.41×10^{4}	2.91×10^{4}
Mass entered the domain due to advection	5.39×10^{3}	5.39×10^{3}
Mass entered the domain due to diffusion	8.73×10^{3}	2.37×10^{4}
Mass entered the domain due to dispersion	9.15×10^{-5}	2.96×10^{-4}
Mass left the domain	4.27×10^{2}	9.63×10^{-1}
Mass stored in aqueous state	1.31×10^{4}	4.68×10^{3}
Mass stored in adsorbed state	0	2.30×10^{4}
Mass consumed in geochemical reaction	6.26×10^{2}	1.45×10^{3}
% normalized mass uptake of CO_{2aq} after 500 years	4.43	4.98
% error in mass balance	5.44×10^{-2}	6.37×10^{-2}

Table 11. Mass [mol] of CO_{2aq} that entered the domain through bottom inflow boundaries of fracture and rock matrix in the reactive transport scenarios 4 and 5.

Scenarios	Scenario-4		Scenario-5	
Bottom inflow boundary	fracture	matrix	fracture	matrix
Total mass entered the domain	5.39×10^{3}	8.73×10^{3}	5.39×10^{3}	2.37×10^{4}
Mass entered the domain due to advection	5.39×10^{3}	0	5.39×10^{3}	0

Mass entered the domain due to diffusion	4.46×10^{-1}	8.73×10^{3}	1.44×10^{0}	2.37×10^{4}
Mass entered the domain due to dispersion	9.15×10^{-5}	0	2.96×10^{-4}	0

Table 12. Mass balance [mol] of Ca^{2+}, mineral calcite and total pore volume of rock matrix in the base-case reactive transport scenarios 4 and 5 after 500 years.

Scenarios	Scenario-4	Scenario-5
Mass [mol] of Ca^{2+} produced in dissolution of mineral calcite	6.22×10^{2}	1.41×10^{3}
Mass [mol] of mineral calcite dissolved	6.25×10^{2}	1.41×10^{3}
Increase in pore volume [m^3]	2.31×10^{-2}	5.21×10^{-2}
% error in mass balance	4.89×10^{-1}	2.35×10^{-1}

Table 13. Mass balance [mol] of CO_{2aq} in various reactive transport scenarios (5.1, 5.2, 5.3, 5.4, and 5a) studied in the sensitivity analysis.

Scenarios	Scenario-5.1	Scenario-5.2	Scenario-5.3	Scenario-5.4	Scenario-5a
Total mass entered the domain	2.59×10^{4}	3.37×10^{4}	4.53×10^{4}	2.06×10^{4}	3.21×10^{4}
Mass entered the domain due to advection	5.39×10^{2}	1.08×10^{4}	5.39×10^{3}	5.39×10^{3}	5.29×10^{3}
Mass entered the domain due to diffusion	2.53×10^{4}	2.29×10^{4}	3.99×10^{4}	1.53×10^{4}	2.68×10^{4}
Mass entered the domain due to dispersion	2.96×10^{-5}	2.52×10^{-4}	5.87×10^{-4}	1.71×10^{-4}	3.04×10^{-4}
Mass left the domain	9.11×10^{-2}	2.75×10^{1}	9.11×10^{-1}	1.85×10^{1}	8.12×10^{-1}
Mass stored in aqueous state	4.13×10^{3}	5.42×10^{3}	2.77×10^{3}	7.41×10^{3}	5.18×10^{3}
Mass stored in adsorbed state	2.03×10^{4}	2.66×10^{4}	4.03×10^{4}	1.22×10^{4}	2.55×10^{4}
Mass converted in geochemical reaction	1.44×10^{3}	1.60×10^{3}	2.23×10^{3}	1.03×10^{3}	1.46×10^{3}
% normalized mass uptake of CO_2 after 500 years	5.58	4.75	4.92	5.00	4.55
% error in mass balance	-3.42×10^{-2}	6.03×10^{-2}	6.40×10^{-2}	6.01×10^{-1}	5.90×10^{-2}

Table 14. Mass balance [mol] of Ca^{2+}, mineral calcite and pore volume of rock matrix in the sensitivity analysis (scenarios 5.1, 5.2, 5.3, 5.4, and 5a).

Scenarios	Scenario-5.1	Scenario-5.2	Scenario-5.3	Scenario-5.4	Scenario-5a
Mass [mol] of Ca^{2+} produced in dissolution of mineral calcite	1.37×10^{3}	1.56×10^{3}	2.13×10^{3}	1.01×10^{3}	1.37×10^{3}
Mass [mol] of mineral	1.37×10^{3}	1.57×10^{3}	2.14×10^{3}	1.02×10^{3}	1.38×10^{3}

calcite dissolved					
Increase in pore volume [m^3]	5.07×10^{-2}	5.79×10^{-2}	7.90×10^{-2}	3.75×10^{-2}	5.10×10^{-2}
% error in mass balance	2.46×10^{-1}	2.11×10^{-1}	2.42×10^{-1}	3.02×10^{-1}	3.60×10^{-1}

1411

1412

1413

1414